Icarus 332 (2019) 111–131

Contents lists available at ScienceDirect

Icarus

journal homepage: www.elsevier.com/locate/icarus

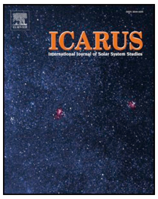

Enceladus's ice shell structure as a window on internal heat production

Douglas J. Hemingway[a,b,*], Tushar Mittal[b]

[a] Department of Terrestrial Magnetism, Carnegie Institution for Science, 5241 Broad Branch Road NW, Washington, D.C. 20015, USA
[b] Department of Earth & Planetary Science, University of California Berkeley, Berkeley, CA 94720, USA

ARTICLE INFO

Keywords:
Enceladus
Interior structure
Ice shell
Tidal heating

ABSTRACT

Its extraordinary level of geologic activity, its potential for habitability, and the prospects of returning samples from its plume of erupting water ice make Saturn's small (~500 km diameter) moon Enceladus a high priority target for future exploration and a key to our developing understanding of icy ocean worlds. The structure of its outer ice shell is particularly important as it relates to the global heat budget, the global-scale response to tidal forces, and the nature of the ongoing eruptions. It is also diagnostic of how and where heat is dissipated internally. Here, using the most recent shape model and a new approach to modeling isostasy, we obtain a shell structure that simultaneously accommodates the shape, gravity, and libration observations and suggests that tidal dissipation near the base of the ice shell is likely an important mode of internal heating. The implied conductive heat loss is greater than the heat loss associated with the eruptions but is nevertheless compatible with the condition of steady state.

1. Introduction

Enceladus's ice shell structure is a key input for understanding the ongoing eruptions (Porco et al., 2006), what governs their timing, and how ocean-to-surface pathways are initiated and sustained (Manga and Wang, 2007; Rudolph and Manga, 2009; Nimmo et al., 2014; Nakajima and Ingersoll, 2016; Ingersoll and Nakajima, 2016; Kite and Rubin, 2016). The thickness and lateral variability of the ice shell also offers clues about the evolution of Enceladus and the future of its internal liquid water ocean. Whereas accretion heat and radiogenic heating are negligible for a body as small as Enceladus, tidal heating due to its forced eccentric orbit can be significant (Fuller et al., 2016; Lainey et al., 2012). How this tidal dissipation is partitioned between the outer ice shell, the subsurface ocean, and the deeper interior will affect the spatial pattern of internal heating and, in turn, the lateral shell thickness variations. Hence, the ice shell's structure also provides a window into the mode of internal heat production. This paper thus has two objectives: 1) to better characterize the interior of Enceladus and, in particular, the structure of its outer ice shell; and 2) to compare this inferred ice shell structure with the expectations from different modes of internal heat production.

The figure of Enceladus exhibits excess polar flattening, departing substantially from the expectation for a body that has relaxed to hydrostatic equilibrium (Nimmo et al., 2011; Tajeddine et al., 2017; Thomas, 2010), but this non-hydrostatic topography is highly compensated, leading the gravitational field to depart only modestly from the hydrostatic expectation (Iess et al., 2014) (Fig. 1). The relationship between the non-hydrostatic gravity and non-hydrostatic topography can be used to estimate the compensation depth, or mean ice shell thickness (e.g., Hemingway et al., 2013; Iess et al., 2014). However, because such analyses focus on relatively small departures from hydrostatic equilibrium, the results are sensitive to the way the hydrostatic components are computed—the usual first order approximations are not sufficient (see McKinnon, 2015); sections 2.2, 3.2.2; Fig. 3).

To determine the shell structure, and interior structure more generally, we carried out a new analysis based on the shape, gravity, and libration observations, incorporating a numerically accurate approach to finding the hydrostatic equilibrium figures (section 2.2; Tricarico, 2014), a new shape model and a new approach to modeling isostasy. Crucially, unlike the early gravity-based interior models for Enceladus (Čadek et al., 2016; Hemingway et al., 2013; Iess et al., 2014; McKinnon, 2015), we do not adopt the common approach of defining isostasy as the requirement of maintaining equal masses in columns of equal width (e.g., Lambeck, 1988). Instead, we adopt a new approach that aims to eliminate lateral pressure gradients at depth (Hemingway and Matsuyama, 2017) (section 2.3). The resulting difference in the best fitting interior models is significant (section 3.2.2; Fig. 3) and reduces the preferred shell thickness to a range that is compatible with the large physical libration amplitude (Fig. 4), resolving the apparent

---

[*] Corresponding author.
E-mail address: dhemingway@carnegiescience.edu (D.J. Hemingway).

https://doi.org/10.1016/j.icarus.2019.03.011
Received 24 October 2018; Received in revised form 20 February 2019; Accepted 13 March 2019

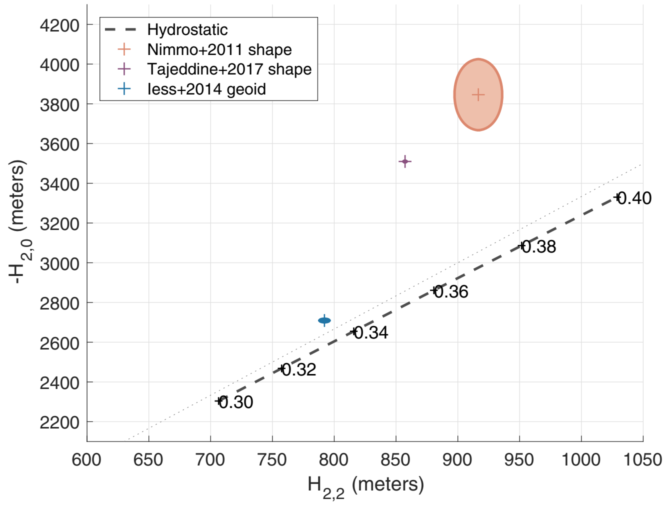

Fig. 1. Comparison of the dominant degree-2 coefficients for published shape models (Nimmo et al., 2011; Tajeddine et al., 2017) and the geoid computed from the measured gravitational field (Iess et al., 2014), with shaded ellipses representing the 1σ uncertainties. The dashed line represents the expectation for a relaxed hydrostatic body (section 2.2; Tricarico, 2014) with moment of inertia factors ranging from 0.3 to 0.4 (the latter corresponding to a uniform interior). The thin dotted line corresponds to a slope of 10/3, consistent with a first-order approximation of the hydrostatic expectation.

discrepancy between some of the early gravity-based results (McKinnon, 2015) and the libration result (Thomas et al., 2016) (see also Beuthe et al., 2016). Whereas, with the recent exception of Čadek et al. (2019), all previously published Enceladus interior models are based on the shape model of Nimmo et al. (2011), we additionally use the newer shape model of Tajeddine et al. (2017). The newer shape model exhibits a smaller departure from the geoid (Fig. 1), leading to a larger preferred compensation depth, or shell thickness, though not so large as to be incompatible with the physical libration amplitude (Fig. 4). For completeness, we undertook a comprehensive exploration of the parameter space (section 3.2), including examination of both Airy (lateral shell thickness variations) and Pratt (lateral density variations) compensation mechanisms, and the possible role of elastic flexure (sections 3.2.3, 3.2.4, and 3.2.5, respectively). We place our results in the context of previous studies in order to emphasize how different observations (including their uncertainties) and different modeling assumptions can affect the conclusions.

Having determined the likely shell structure and the range of possibilities that are compatible with the observations (section 3), we then discuss internal heat production (section 4) and compare the inferred shell structure with the outcomes expected if the internal dissipation is primarily concentrated in the core, the ocean, or the ice shell. For the latter case, we use a thin-shell tidal heating model (section 2.8) to compute the spatial pattern of tidal dissipation within the ice shell (Fig. 11a) and the resulting equilibrium ice shell structure (Fig. 11c). We show that the inferred ice shell structure (Fig. 11d) is broadly consistent with the expectations from tidal dissipation in the ice shell and we argue that the inferred shell structure is not as readily explainable if the tidal dissipation is focussed primarily within the ocean or the core (section 4.2). Our model may thus be regarded as an alternative to the Choblet et al. (2017) model, which favors dissipation within the core; we discuss the advantages and disadvantages of each model in sections 4.2 and 4.3. We also show that maintaining the inferred shell structure near steady state requires internal heat production in the range of 20 − 40 GW, which is marginally compatible with the dissipation implied by recent astrometric observations (Lainey et al., 2012, 2017), permitting a long-lived internal ocean (section 4.1).

Section 2 provides details on the main methods used in our analysis. In section 3, we explore the parameter space and illustrate how it is constrained by the shape, gravity, and libration observations, with the results being summarized in section 3.3. In section 4, we discuss internal heat production, the heat budget, and the results of our tidal dissipation model. Finally, concluding remarks are given in section 5.

2. Methods

2.1. Gravitational field

The gravitational field of Enceladus was measured through radio Doppler tracking of the *Cassini* spacecraft during three dedicated gravity flybys (Iess et al., 2014). The external gravitational potential can be expressed as a linear combination of spherical harmonic functions as follows

$$U(r,\theta,\phi) = -\frac{GM}{r}\sum_{l=0}^{\infty}\sum_{m=-l}^{l}\left(\frac{R_{\mathrm{ref}}}{r}\right)^{l} C_{lm} Y_{lm}(\theta,\phi) \tag{1}$$

where the potential is evaluated at radius r, colatitude θ, and longitude ϕ, where C_{lm} represents the degree-l and order-m dimensionless gravitational potential coefficients at some reference radius (R_{ref}), and where $Y_{lm}(\theta,\phi)$ are the spherical harmonic functions (e.g., Wieczorek, 2015). The point mass term is captured by the fact that $C_{00} \equiv 1$. In the center of mass frame, the degree-1 coefficients are zero. Note that whereas Iess et al. (2014) originally reported their coefficients (C_{lm}) for a reference radius of $R_{\mathrm{ref}} = 254.2$ km (McKinnon, 2015), we use $R_{\mathrm{ref}} = 252.1$ km or $R_{\mathrm{ref}} = 252.22$ km corresponding to the older (Nimmo et al., 2011; Thomas, 2010) and newer (Tajeddine et al., 2017) shape models, respectively. Note that we sometimes follow the convention of representing the zonal gravity coefficients as $J_l = -C_{l0}$.

The geoid is an equipotential surface corresponding to the mean potential at the reference radius, $U_{\mathrm{ref}} = -GM/R_{\mathrm{ref}}$, and is given by

$$N(\theta,\phi) = R_{\mathrm{ref}}\sum_{l=0}^{\infty}\sum_{m=-l}^{l} C_{lm} Y_{lm}(\theta,\phi) - \frac{5}{6}\frac{\omega^2 R_{\mathrm{ref}}^2}{g} Y_{20}(\theta,\phi) + \frac{1}{4}\frac{\omega^2 R_{\mathrm{ref}}^2}{g} Y_{22}(\theta,\phi) \tag{2}$$

where the latter two terms account for the combined tidal and rotational potentials, where $g = GM/{R_{\mathrm{ref}}}^2$ is the mean surface gravity. We emphasize that the spherical harmonic functions Y_{20} and Y_{22} are not normalized here.

We model Enceladus as a two- or three-layer body with near spherical symmetry. Departure from spherical symmetry occurs due to tidal/rotational deformation plus the elastically/isostatically supported nonhydrostatic topography. For the i^{th} layer, the departure from spherical symmetry (i.e., the spherically-referenced topography) is described by H_{ilm}. In general, the i^{th} layer may also exhibit lateral variations in density, described by $\delta\rho_{ilm}$.

The gravitational potential can be written

$$U(r,\theta,\phi) = -4\pi G\left(\frac{1}{r}\int_0^r \rho(r')r'^2 dr' + \int_r^R \rho(r')r' dr'\right) + \sum_{l=1}^{\infty}\sum_{m=-l}^{l} U_{lm}(r) Y_{lm}(\theta,\phi) \tag{3}$$

where $\rho(r')$ describes the mean (spherically symmetric) radial density structure and where the coefficients describing the asymmetric part of the potential, U_{lm}, are given by

$$U_{lm}(r) = -\frac{4\pi G r}{2l+1}\left(\sum_{i_{\mathrm{below}}} \Delta\rho_i H_{ilm}^{+}\left(\frac{R_i}{r}\right)^{l+2} + \sum_{i_{\mathrm{above}}} \Delta\rho_i H_{ilm}^{-}\left(\frac{r}{R_i}\right)^{l-1} + \int_{r'=0}^{r} \delta\rho_{lm}(r')\left(\frac{r'}{r}\right)^{l+2} dr' + \int_{r'=r}^{R_t} \delta\rho_{lm}(r')\left(\frac{r}{r'}\right)^{l-1} dr'\right) \tag{4}$$

where $\Delta\rho_i$ is the density contrast between layer i and the layer above it, and R_i is the mean outer radius of the i^{th} layer; R_t is the mean outer radius of the top layer. The summation performed over i_{below} includes only the layers whose outer radius is below (or at) the point of interest (i.e., $r \geq R_i$) and the summation performed over i_{above} includes only layers whose outer radius is above the point of interest (i.e., $r < R_i$). Layers with laterally variable density will have non-zero density anomaly expansion coefficients ($\delta\rho_{lm}$) and layers with laterally variable topography at their upper boundaries will have non-zero topography expansion coefficients (H_{ilm}). Eq. (4) neglects the small contributions from terms in $\delta\rho_{lm}H_{ilm}$.

Because the amplitude of the long wavelength topography can be substantial compared with the size of Enceladus, we also include the terrain- or finite-amplitude correction when evaluating the potential arising from each layer's topography. This correction is denoted in Eq. (4) by the superscripts $^{+}$ or $^{-}$, indicating that the topography coefficients have been adjusted (as described below) such that the resulting potential accounts for the finite amplitude of the topography. This is important mainly for the large basal topography describing the isostatic roots in the case of our Airy compensation models. For Enceladus, and assuming ice shell and ocean densities of 925 kg/m^3 and 1020 kg/m^3, respectively, the J_2 part of the gravity field could be underestimated by ~5% if this finite-amplitude correction is not included. Here we follow Wieczorek and Phillips, (1998), but with slightly modified notation. We evaluate the topography of the i^{th} layer, $H_i(\theta, \phi)$, measured with respect to the sphere R_i, and raise that topography to the n^{th} power. The result is then expanded in spherical harmonics, with the coefficients denoted H_{nilm}. That is,

$$H_i^n(\theta, \phi) = \sum_{l=1}^{\infty}\sum_{m=-l}^{l} H_{nilm} Y_{lm}(\theta, \phi). \tag{5}$$

For $r \geq R_i$, we then compute the finite-amplitude-adjusted topography as

$$H_{ilm}^{+} = R_i \sum_{n=1}^{l+3} \frac{H_{nilm}}{R_i^n} \frac{\prod_{j=1}^{n}(l+4-j)}{n!(l+3)} \tag{6}$$

where the first term in the summation is simply the true topography and the remaining terms constitute the small adjustments required to obtain the correct potential via Eq. (4). The identical result is obtained by combining Eqs. (9) and (10) of Wieczorek and Phillips (1998).

When $r < R_i$, we instead compute the finite-amplitude-adjusted topography as

$$H_{ilm}^{-} = R_i \sum_{n=1}^{\infty} \frac{H_{nilm}}{R_i^n} \frac{\prod_{j=1}^{n}(l+j-3)}{n!(l-2)} \tag{7}$$

which, when combined with Eq. (4) gives the same result as combining Eqs. (11) and (12) of Wieczorek and Phillips (1998).

In practice, our analysis here always involves evaluating the potential at the reference radius ($r = R_{\text{ref}}$), so Eq. (4) reduces to

$$U_{lm}(r) = -\frac{4\pi G r}{2l+1} \sum_i \left(\Delta\rho_i H_{ilm}^{+} \left(\frac{R_i}{r}\right)^{l+2} + \frac{\delta\rho_{ilm}}{r^{l+2}} \left(\frac{R_{ti}^{l+3} - R_{bi}^{l+3}}{l+3} \right) \right) \tag{8}$$

where R_{ti} and R_{bi} are the mean radii corresponding to, respectively, the top and bottom of the i^{th} layer. The latter term is generally zero except when we allow for Pratt-type isostatic compensation. Although Eq. (8) is only strictly valid at radii outside the highest standing topography (Wieczorek and Phillips, 1998), we will nevertheless use it to compute a notional potential at the reference radius ($r = R_{\text{ref}}$) for purposes of comparison with the measured gravitational potential, which is often expressed at the mean outer radius rather than at some arbitrary larger radius outside all the topography.

We treat each layer's shape (H_{ilm}) as the sum of a hydrostatic equilibrium figure and a non-hydrostatic component that is presumed to be supported isostatically and/or elastically

$$H_{ilm} = H_{ilm}^{\text{hyd}} + H_{ilm}^{\text{nh}}. \tag{9}$$

We compute the hydrostatic term (H_{ilm}^{hyd}) as described in section 2.2. The non-hydrostatic terms (H_{ilm}^{nh}) may be constrained by observations or inferred from our isostasy model as described in section 2.3.

2.2. Hydrostatic equilibrium figures

For each of our models, we begin by computing hydrostatic equilibrium figures for each layer. For synchronous satellites, the hydrostatic equilibrium figure is a function of the spatially varying combined tidal and rotational potential, given by

$$V(\theta, \phi) = \omega^2 R^2 \left(\frac{5}{6} Y_{20}(\theta, \phi) - \frac{1}{4} Y_{22}(\theta, \phi) \right) \tag{10}$$

where ω and R are the mean rotation rate and radius of Enceladus. This approximation assumes only that the tidal potential can be well represented by a degree-2 function and that the mass of the parent body is much larger than the mass of the satellite (a very good assumption in this case since Saturn is more than 10^6 times as massive as Enceladus).

The resulting equilibrium figure is typically computed using the first order approximation

$$H^{\text{hyd}}(\theta, \phi) = \frac{V(\theta, \phi)}{g} h_f \tag{11}$$

where g is the surface gravity (radial gradient of the potential), and h_f is the fluid (or secular) Love number, which can be related to the moment of inertia—and thus the internal mass distribution—via the Radau-Darwin equation (Darwin, 1899; Murray and Dermott, 1999). This approach was followed in obtaining the first Enceladus interior models based on gravity data (Iess et al., 2014). However, this approach can lead to significant errors when the results depend on small departures from hydrostatic equilibrium, especially in the case of fast-rotating bodies like Enceladus (McKinnon, 2015; Tricarico, 2014) (see section 3.2.2).

Using a fourth order recursive solution developed by Tricarico (2014) for two-layer bodies, McKinnon (2015) re-examined the analysis of Iess et al. (2014), obtaining an updated interior structure model. The Tricarico (2014) formulation adopts the same assumptions about the tidal/rotational disturbing potential captured in Eq. (10), but retains higher order terms in computing the resulting equilibrium figure, which is approximated as a triaxial ellipsoid. We follow McKinnon (2015) in using the Tricarico (2014) formulation except that, instead of the fourth order recursive solution, which is limited to two-layer bodies, we use the numerical solution, which accommodates an arbitrary number of layers. This approach delivers exact numerical solutions for triaxial ellipsoidal equipotential surfaces resulting from the tidal/rotational disturbing potential of Eq. (10). We represent the resulting triaxial ellipsoidal figures as strictly degree-2 shapes with power at only $m = 0$ and $m = 2$. The reference hydrostatic equilibrium shapes for the i^{th} layer are thus represented by just two coefficients: H_{i20}^{hyd} and H_{i22}^{hyd}. In reality, these triaxial ellipsoids have some small additional power at all other even harmonics, but for purposes of making comparisons with the observed gravity, we cannot presently make use of anything beyond $l = 3$, and hence a degree-2 hydrostatic figure is sufficient.

Because the non-hydrostatic topography, which is the focus of much of this analysis, is sensitive to small changes in the hydrostatic equilibrium figure, these improvements over first order theory can be important. For example, assuming a moment of inertia of $0.335MR^2$ for Enceladus (Iess et al., 2014), first order theory underestimates the hydrostatic H_{22}^{hyd} by ~4% compared with the numerical solution of Tricarico (2014), leading to a ~30% overestimate of the non-hydrostatic component, H_{22}^{nh}. The fourth order solution yields non-hydrostatic topography that is within 1% of the numerical results, but an advantage of the numerical approach is that it avoids having to treat the combined ocean and ice shell as a single layer for purposes of computing hydrostatic equilibrium figures, and that it delivers equilibrium shapes for not only the core and surface, but also for the ocean/ice interface.

2.3. Isostatically supported non-hydrostatic topography

For our three-layer models, we ensure that the non-hydrostatic surface topography ($H_{\text{tlm}}^{\text{nh}} = H_{\text{tlm}}^{\text{obs}} - H_{\text{tlm}}^{\text{hyd}}$) is supported through a combination of elastic forces and isostasy, either in the Airy sense of lateral shell thickness variations or in the Pratt sense of lateral density variations.

For the end member case of Airy isostasy, the topography is supported buoyantly by isostatic roots, i.e., non-hydrostatic topography at the base of the ice shell ($H_{\text{blm}}^{\text{nh}}$). For clarity, we use the subscripts t and b to represent the top and bottom of the ice shell, respectively, rather than numerical indices which would depend on the numbering scheme. We set the surface relief to match the observations and compute the relief at the base of the ice shell as (Hemingway and Matsuyama, 2017)

$$H_{blm}^{\text{nh}} = -H_{tlm}^{\text{nh}} \frac{\rho_{\text{ice}}}{\Delta\rho}\left(\frac{g_t}{g_b}\right) \tag{12}$$

where ρ_{ice} is the density of the ice, $\Delta\rho$ is the density contrast at the ice/ocean interface, and where g_t and g_b are the gravitational accelerations at the top and bottom of the ice shell, respectively.

Under the opposite end member assumption of Pratt isostasy (not explicitly modeled in previous work on Enceladus), the high standing non-hydrostatic topography is associated with systematically lower crustal densities. The lateral density variations required to achieve isostatic equilibrium, again following the approach of Hemingway and Matsuyama (2017), are given by

$$\delta\rho_{lm} \approx -\rho_{\text{ice}}\left(\frac{H_{tlm}^{\text{nh}}}{R_t - R_b}\right)\left(\frac{2}{1 + \frac{g_b}{g_t}}\right) \tag{13}$$

where ρ_{ice} is the mean density of the icy crust.

Eqs. (12) and (13) account for the spherical geometry of the isostasy problem in a way that assures approximately equal pressures along equipotential surfaces at depth (Hemingway and Matsuyama, 2017). Note that Eq. (12) differs from the corresponding expressions in previous studies of Enceladus's ice shell (e.g., Iess et al., 2014; McKinnon, 2015; Čadek et al., 2016) and other similar work. Many of these studies follow the convention of defining isostasy as requiring equal masses in columns (or cones) of equal width (e.g., Lambeck, 1988). However, Hemingway and Matsuyama (2017) showed, via integration of the hydrostatic equation, that this "equal masses" requirement does not produce an equilibrium condition and can lead to a significantly larger estimate of the amplitude of the required isostatic roots ($H_{\text{blm}}^{\text{nh}}$). Consider, for example, the approach of Čadek et al. (2016), which is similar to the Lambeck (1988) model except that they also allow for the radial variation in gravity. In comparison to the Hemingway and Matsuyama (2017) model, Eq. (1) of Čadek et al. (2016), assuming complete compensation, leads to a basal topography amplitude that is larger by a factor of $(R_t/R_b)^2$ where R_t and R_b are the mean radii at the top and bottom of the ice shell, respectively. This factor can be significant in the case of Enceladus since the mean shell thickness could be a substantial fraction of the total radius. For example, if the mean ice shell thickness is 25 km, then compared with our approach, Eq. (1) of Čadek et al., 2016) implies a basal topography amplitude that is larger by ~23%.

As discussed by Hemingway and Matsuyama (2017), however, it should be noted that the principle of isostasy as a static equilibrium condition may be flawed in that it assumes a lithosphere that is too weak to support any vertical shear stresses, and yet is simultaneously strong enough to resist viscous relaxation. Ideally, the full dynamic nature of the system should be taken into account, as has been done in some recent work (e.g., Čadek et al., 2017, 2019). These dynamic models, however, entail a number of additional assumptions and simplifications of their own. In particular, the Čadek et al., (2017); Čadek et al. (2019) models do not explicitly address the effects of the lateral pressure gradients within the ocean. A self-consistent dynamic model that simultaneously accounts for the behavior of everything from the highly viscous ice to the dynamics of the inviscid ocean is desirable. For the present study, however, we accept the limitations of the concept of a static isostasy and we primarily make use of the Hemingway and Matsuyama (2017) model, though we also show results from the Lambeck (1988) model as a point of comparison in section 3.2.2.

Although the Hemingway and Matsuyama (2017) approach to Airy isostasy differs in detail from the minimum stress isostasy approach of Beuthe et al. (2016), the two share the basic premise that the topography is supported mainly through buoyancy rather than lithospheric stresses, and neither method involves the requirement of equal masses in columns (or cones) of equal width. Using the Nimmo et al. (2011) shape model, our preferred ice shell and ocean thicknesses do not differ significantly from those of Beuthe et al. (2016) (whereas they obtain shell and ocean thicknesses of 19 − 27 km and 34 − 42 km, respectively, we obtain 21 − 25 km and 37 − 44 km, respectively; Table 2).

2.4. Flexural support

Whereas Eq. (12) assumes complete Airy compensation, we also consider the possibility of additional elastic flexural support. (We do not consider the scenario in which flexural support is combined with partial Pratt isostasy.) Treating the lithosphere as a uniform thin elastic shell (Kraus, 1967; Turcotte et al., 1981; Willemann and Turcotte, 1982), it can be shown (Appendix A) that Eq. (12) generalizes to

$$H_{blm}^{\text{nh}} = -H_{tlm}^{\text{nh}} \frac{\rho_{\text{ice}}}{\Delta\rho}\frac{g_t}{g_b}\left(\frac{1}{1 + \frac{\zeta}{\Delta\rho g_b}}\right) \tag{14}$$

when the loading is entirely from the top of the shell, or

$$H_{blm}^{\text{nh}} = -H_{tlm}^{\text{nh}} \frac{\rho_{\text{ice}}}{\Delta\rho}\frac{g_t}{g_b}\left(\frac{1}{1 + \frac{\zeta}{\rho_{\text{ice}} g_t}}\right)^{-1} \tag{15}$$

when the loading is entirely from the base of the shell. The quantity ζ has units of force per unit volume and serves as a shorthand for the flexural rigidity at a particular wavelength (spherical harmonic degree l), and is given by (see Appendix A)

$$\zeta(l, R, E, T_e, \nu) = \frac{ET_e}{R^2}\left(\frac{\frac{T_e^2}{R^2 12(1-\nu^2)}(l^3(l+1)^3 - 4l^2(l+1)^2 + 4l(l+1)) + l(l+1) - 2}{l(l+1) - (1-\nu)}\right) \tag{16}$$

where T_e is the effective elastic thickness, and E and ν are the Young's modulus and Poisson's ratio for the icy lithosphere. R is the radius of the thin elastic shell, which we take to be the body's outer radius. The quantities in parentheses in Eqs. (14) and (15) may be regarded as compensation factors. In both cases, decreasing rigidity ($T_e \to 0$, $\zeta \to 0$) leads the compensation factor to approach unity, at which point both Eqs. (14) and (15) reduce to Eq. (12). For non-zero rigidity, the compensation factors mean different things for the cases of bottom and top loading. Increasing shell rigidity (increasing T_e and therefore ζ) reduces the compensation factor in either case, but this implies reduced basal topography in the case of top loading, or reduced surface topography in the case of bottom loading (see section 3.2.5).

2.5. Libration amplitude

Due to its eccentric orbit, Enceladus moves relatively faster near pericenter and slower near apocenter. This results in small misalignments between the long (tidally bulged) axis of Enceladus and the line connecting Enceladus with Saturn. This misalignment means that Saturn exerts gravitational torques on Enceladus's tidal bulge, forcing Enceladus to experience physical librations—small oscillations in its otherwise steady rotation rate. The amplitude of these forced physical

Table 1

Observed gravity coefficients and their uncertainties (Iess et al., 2014), along with the corresponding uncertainties from the shape models, their effect on the model gravity uncertainties, computed via Eq. (25), and the combined effect (σ_{lm}). The gravity coefficients in the upper and lower parts of the table differ slightly because each is expressed at a reference radius corresponding to the mean radius for each shape model: $R_{\mathrm{ref}} = 252.1$ km and $R_{\mathrm{ref}} = 252.22$ km for the Nimmo et al. (2011) and Tajeddine et al. (2017) shape models, respectively. The assumed shell density is $\rho_{\mathrm{shell}} = 925$ kg/m^3, and all coefficients are unnormalized.

Shape model	l, m	$C_{lm}{}^{\mathrm{grav}}$	$\sigma_{lm}{}^{\mathrm{grav}}$	$H_{lm}{}^{\mathrm{topo}}$	$\sigma_{lm}{}^{\mathrm{topo}}$	$\sigma_{lm}{}^{\mathrm{topo}^*}$	σ_{lm}
Nimmo et al. (2011)	2, 0	-5526×10^{-6}	35.4×10^{-6}	−3846 m	178.9 m	244.8×10^{-6}	247.3×10^{-6}
	2, 2	1576×10^{-6}	15.9×10^{-6}	917 m	19.4 m	26.5×10^{-6}	30.9×10^{-6}
	3, 0	118×10^{-6}	23.4×10^{-6}	384 m	4.8 m	4.7×10^{-6}	23.9×10^{-6}
Tajeddine et al. (2017)	2, 0	-5521×10^{-6}	35.4×10^{-6}	−3510 m	3.9 m	5.3×10^{-6}	35.8×10^{-6}
	2, 2	1574×10^{-6}	15.8×10^{-6}	857 m	1.3 m	1.7×10^{-6}	15.9×10^{-6}
	3, 0	118×10^{-6}	23.4×10^{-6}	420 m	4.5 m	4.4×10^{-6}	23.8×10^{-6}

librations is a function of the orbital eccentricity and moments of inertia of Enceladus. In the case of a multi-layer body, with all the layers physically coupled to one another, the physical libration amplitude is given by (e.g., Murray and Dermott, 1999)

$$\gamma = \frac{2e}{1 - (n/\omega_0)^2} \tag{17}$$

where e is Enceladus's orbital eccentricity, n is its mean motion, and ω_0 is its natural frequency, given by

$$\omega_0 = n\sqrt{\frac{3(B-A)}{C}} \tag{18}$$

where $A < B < C$ are the principle moments of inertia. These are captured in the moon's dynamical triaxiality, given by

$$\frac{B-A}{C} = \frac{\sum_i \Delta\rho_i (a_i^2 - b_i^2) a_i b_i c_i}{\sum_i \Delta\rho_i (a_i^2 + b_i^2) a_i b_i c_i} \tag{19}$$

where $\Delta\rho_i$ is the density contrast between the i^{th} layer and the layer above it, and where a_i, b_i and c_i are, respectively, the semi-major, semi-intermediate, and semi-minor axes corresponding to the i^{th} layer, which is taken to be a triaxial ellipsoid.

In the special case of a three layer body in which the intermediate layer is taken to be a global liquid layer that physically decouples the core from the outer ice shell, the physical libration amplitude is instead given by (e.g., Richard et al., 2014; Thomas et al., 2016)

$$\gamma = \frac{2e\left[K_{\mathrm{s}}(K_{\mathrm{c}} + 2K_{\mathrm{int}} - n^2 C_{\mathrm{c}}) + 2K_{\mathrm{int}}K_{\mathrm{c}}\right]}{C_{\mathrm{s}}C_{\mathrm{c}}(n^2 - \omega_1^2)(n^2 - \omega_2^2)} \tag{20}$$

where C_{s} and C_{c} are the separate polar moments of inertia for the shell and core, respectively. In this case, there are multiple separate torques to consider: K_{s} and K_{c} are the amplitudes of the effective torques applied by Saturn on the shell and core, respectively, and are mainly functions of moment of inertia differences *(B-A)* in those layers. Meanwhile, K_{int} is the amplitude of the effective torque applied by the core on the shell, and is a function of the shapes and density contrasts at the core/ocean boundary and at the ocean/shell boundary (Richard et al., 2014). Finally, ω_1 and ω_2 are the system's natural frequencies. For further details, see Richard et al. (2014); Thomas et al. (2016); Van Hoolst et al. (2009, 2013). Whereas the core is assumed to be hydrostatic (though see 3.2.6), the outer shape of the ice shell comes directly from the observations (Nimmo et al., 2011; Tajeddine et al., 2017) and the shape of the ice/ocean interface is obtained as described in section 2.3 or 2.4. Uncertainties in the outer shape model are handled as described in section 2.6 below. Consistent with Thomas et al. (2016), we do not consider the effects of diurnal tidal variations in the figures, which have been shown to reduce the libration amplitude, at least in the case of large ocean worlds (Van Hoolst et al., 2013); the effect is probably small for Enceladus (Van Hoolst et al., 2016).

2.6. Goodness of fit

For each of our models, we explore the two-, three-, or four-dimensional parameter space exhaustively (with steps of 1 km in layer thicknesses, 25 kg/m^3 in layer densities, and 10 m in elastic thicknesses) in order to find the best fitting parameters. We use the techniques described above to develop interior models over the full grid, and then compute the resulting gravitational field using Eq. (8) and the libration amplitude using Eqs. (17) or (20), depending on whether a decoupling ocean is present. At each point in the parameter space, we then quantify the goodness of fit using the Mahalanobis distance, given by

$$L = \sqrt{(\mathbf{X} - \mathbf{Y})^T \mathbf{\Sigma}^{-1} (\mathbf{X} - \mathbf{Y})} \tag{21}$$

where $\boldsymbol{X}$ is a vector containing the model results (gravitational potential coefficients and libration amplitude) and where $\boldsymbol{Y}$ is a vector containing the observations (the observed gravitational potential coefficients (Iess et al., 2014) and libration amplitude (Thomas et al., 2016)), and where it is understood that only the measurably non-zero gravitational potential coefficients are included (i.e., C_{20}, C_{22}, C_{30}, in the present case). The covariance matrix, Σ, captures the uncertainties in both the model and the observations, and is given by

$$\mathbf{\Sigma} = \mathbf{\Sigma}^{\mathrm{obs}} + \mathbf{\Sigma}^{\mathrm{model}} \tag{22}$$

where Σ^{obs} is the covariance matrix corresponding to the observations, consisting of the estimated gravitational potential coefficients covariances (D. Durante & L. Iess, personal communication) and the variance of the estimated libration amplitude (Thomas et al., 2016); the libration amplitude and gravitational potential coefficients are assumed to be uncorrelated. Likewise, Σ^{model} is a covariance matrix comprising model uncertainties. Uncertainties in the model gravitational potential arise from the propagation of uncertainties from the shape models (Nimmo et al., 2011; Tajeddine et al., 2017) through Eq. (8). Similarly, uncertainties in the model libration amplitude arise from propagating the shape model uncertainties through the libration calculation described in section 2.5. Because it is impractical to directly propagate these uncertainties every time the libration amplitude is computed from the model, we instead used a Monte-Carlo approach to determine how the computed libration amplitude uncertainty is related to the shape model uncertainties, and then used a conservative fixed value for each shape model. The Nimmo et al. (2011) shape model uncertainties (see Table 1) translate to a 1σ uncertainty of $<0.004°$ in the computed libration amplitude while the Tajeddine et al. (2017) uncertainties translate to a 1σ uncertainty of $<0.00025°$. Squaring this value gives the last term in Σ^{model}. Since the shape model coefficients were assumed to be independent (i.e., covariances were not published by either Nimmo et al. (2011) or Tajeddine et al. (2017)), we must accept the approximation that Σ^{model} is diagonal.

Assuming the errors are normally distributed, we compute the probability density at every point in the parameter space as

$$f(\boldsymbol{X}, \boldsymbol{Y}, \mathbf{\Sigma}) = \frac{1}{\sqrt{|\Sigma|(2\pi)^k}} e^{-L^2/2} \tag{23}$$

where k is the number of degrees of freedom, which we take to be the number of measurable gravitational potential coefficients plus the

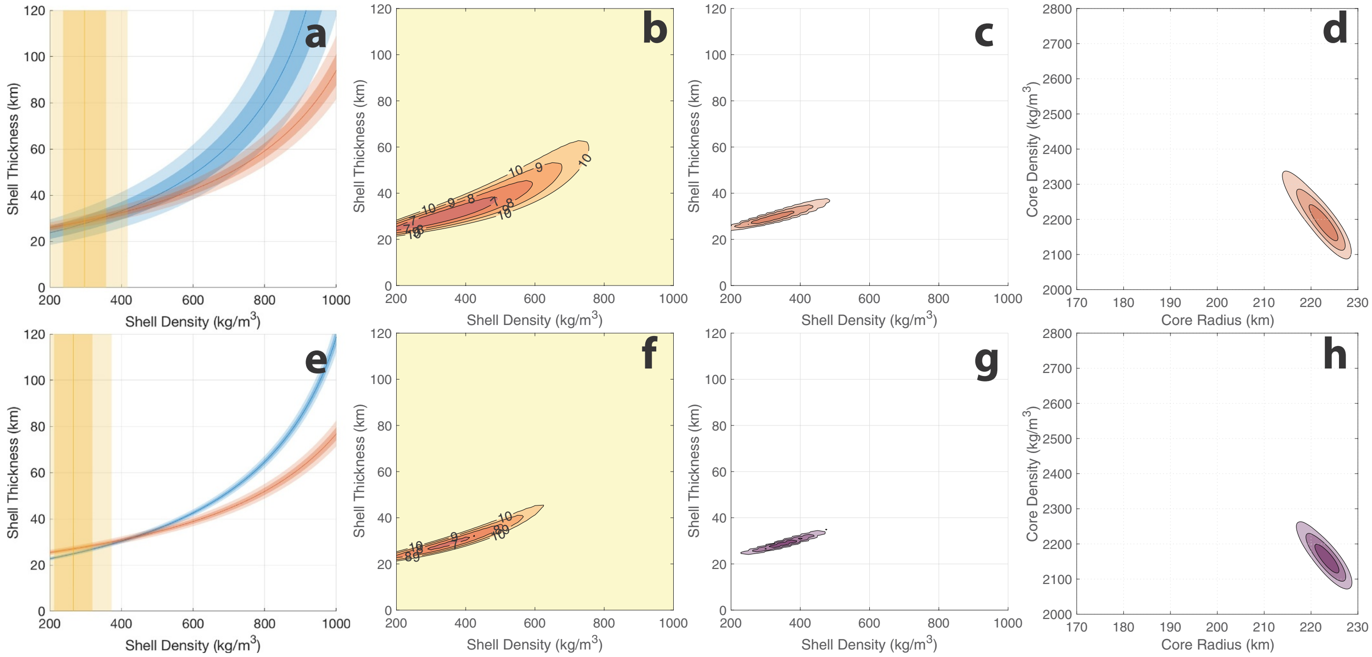

Fig. 2. Misfits and probability densities across the parameter space assuming a two-layer model, and comparing results derived from the shape models of (a–d) Nimmo et al. (2011) and (e–h) Tajeddine et al. (2017). (a,e) Lines indicate combinations of shell thickness and density that satisfy the observed J_2 (blue), C_{22} (red), or J_3 (gold) dimensionless gravitational potential coefficients (Iess et al., 2014), with shaded bands indicating 1σ (dark) and 2σ (pale) bounds from combined shape and gravity model uncertainties (section 2.6). (b,f) Misfit between the model and the observations, given by Eq. (21). (c,g) 68% (dark), 95% (intermediate), and 99.7% (pale) confidence contours showing shell thicknesses and densities that best account for the observed gravitational potential, and (d,h) corresponding core radius and density (section 2.6). The minimum misfits are $L = 6.1$ and $L = 6.7$ for the Nimmo et al. (2011) and Tajeddine et al. (2017) shape models, respectively, but require unreasonably small ice shell densities. (For interpretation of the references to color in this figure legend, the reader is referred to the web version of this article.)

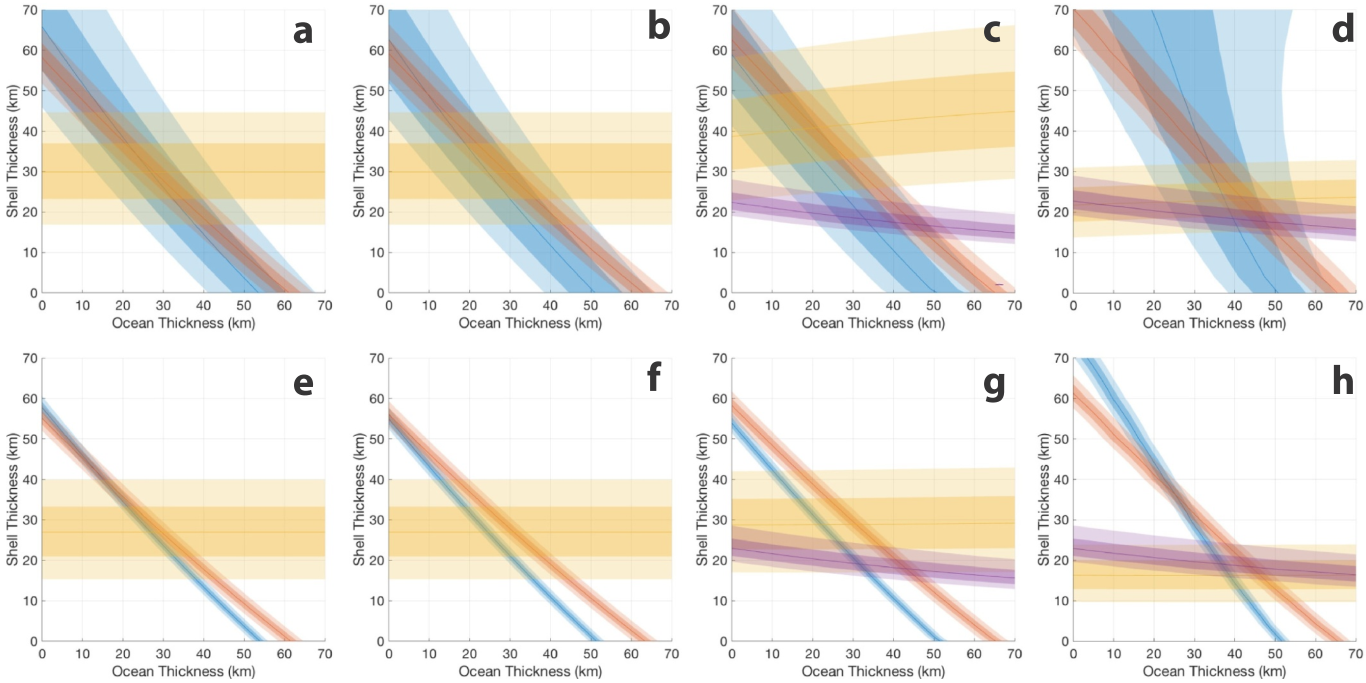

Fig. 3. Sensitivity to methodological choices, adopting the shape models of (a–d) Nimmo et al. (2011) or (e–h) Tajeddine et al. (2017). The curves illustrate the parts of the parameter space that satisfy the observed J_2 (blue), C_{22} (red), or J_3 (gold) dimensionless gravitational potential coefficients (Iess et al., 2014), and the observed libration amplitude (purple) (Thomas et al., 2016), with shaded bands indicating 1σ (dark) and 2σ (pale) uncertainties (section 2.6). (a,e) Results obtained following the approach of Iess et al. (2014). (b,f) Results obtained following the approach of McKinnon (2015), wherein the equilibrium figure is computed following the approach of Tricarico (2014). (c,g) Results obtained with our three-layer model, which includes the finite amplitude correction (Wieczorek and Phillips, 1998), and retaining the "equal masses" conception of isostasy used in earlier studies. (d,h) Results obtained when the "equal masses" isostatic model is replaced with the "equal pressures" model of Hemingway and Matsuyama (2017). For all panels, we assume $\rho_{\text{shell}} = 925$ kg/m^3 and $\rho_{\text{ocean}} = 1020$ kg/m^3. The minimum misfits when using the Nimmo et al. (2011) shape model are: (a) $L = 0.4$, (b) $L = 1.5$, (c) $L = 3.3$, (d) $L = 1.6$. When using the Tajeddine et al. (2017) shape model, they are: (e) $L = 1.3$, (f) $L = 2.9$, (g) $L = 6.0$, (h) $L = 3.7$. (For interpretation of the references to color in this figure legend, the reader is referred to the web version of this article.)

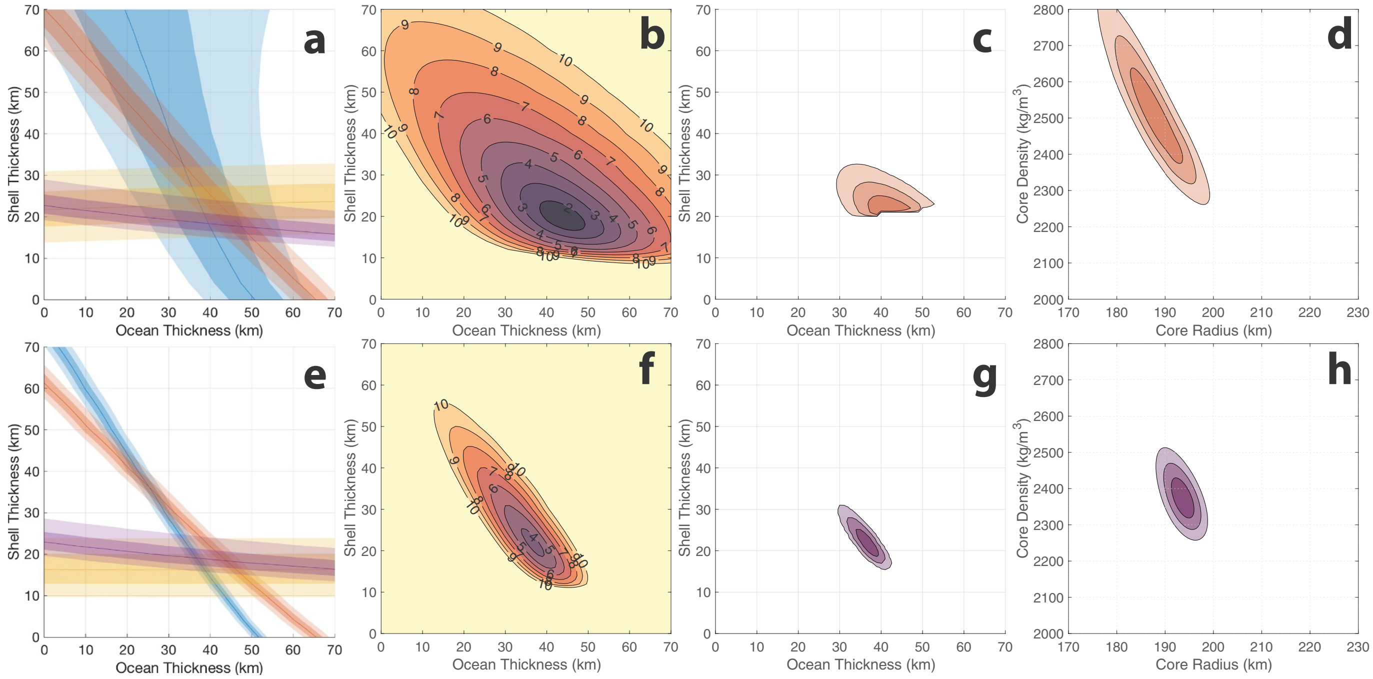

Fig. 4. Misfits and probability densities across the parameter space assuming Airy compensation, with $\rho_{\rm shell} = 925$ kg/m^3 and $\rho_{\rm ocean} = 1020$ kg/m^3, and comparing results derived from the shape models of (a–d) Nimmo et al. (2011) and (e–h) Tajeddine et al. (2017). (a,e) Lines indicate combinations of shell and ocean thicknesses that satisfy the observed J_2 (blue), C_{22} (red), or J_3 (gold) dimensionless gravitational potential coefficients (Iess et al., 2014), and the observed libration amplitude (purple) (Thomas et al., 2016), with shaded bands indicating 1σ (dark) and 2σ (pale) uncertainties on the estimated values (section 2.6); same as Fig. 3d, h. (b,f) Misfit between the model and the observations, given by Eq. (21). (c,g) 68% (dark), 95% (intermediate), and 99.7% (pale) confidence contours showing ice shell and ocean thicknesses that best account for the observed gravitational potential and libration amplitude, and (d,h) corresponding core radius and density. The sharp lower boundary on mean shell thickness in (c) is the result of excluding parts of the parameter space where the south polar shell thickness is less than zero; the same criterion is applied in (g) but the effect is subtle because the south polar topographic depression is less pronounced in the Tajeddine et al. (2017) shape model. The minimum misfits are $L = 1.6$ and $L = 3.7$ for the Nimmo et al. (2011) and Tajeddine et al. (2017) shape models, respectively. (For interpretation of the references to color in this figure legend, the reader is referred to the web version of this article.)

libration amplitude (γ). In the present case, $k = 4$ (i.e., C_{20}, C_{22}, C_{30}, γ).

We do not attempt to evaluate the likelihood of each model in absolute terms, which would require some assumptions about prior probabilities across the parameter space. Instead, the contours in Figs. 2, 4, 6, S1, S2, S3, and S4, are chosen such that they enclose 68.27% (dark), 95.45% (intermediate), and 99.73% (pale) of the probability density-weighted volume of the explored parameter space, with the implicit assumption that the cumulative probability within this volume is equal to unity. Hence, our confidence contours show only the relative likelihood of the model parameters given each particular set of model assumptions (i.e., the chosen shape and gravity models, the chosen isostasy model, the ranges of layer densities considered, and the range of allowed elastic support). For our three-layer Airy models, however, we require that the ice shell and ocean thickness be everywhere greater than zero. This is accomplished by forcing the probability density to zero in parts of the parameter space where this condition is violated.

The shaded bands in Figs. 2, 3, 4, 6, and 8 illustrate the combined 1σ or 2σ uncertainties, neglecting any correlation between the terms. That is, the width of each dark band is the standard deviation, given by the square root of the diagonal elements of the combined covariance matrix Σ. Equivalently, the uncertainties relating to the gravitational potential coefficients are given by

$$\sigma_{lm} = \sqrt{(\sigma_{lm}^{\rm grav})^2 + (\sigma_{lm}^{\rm topo*})^2} \tag{24}$$

where $\sigma_{\rm lm}^{\rm grav}$ are the uncertainties on the measured coefficients (Iess et al., 2014) and where $\sigma_{lm}^{\rm topo*}$ are the uncertainties in the model potential field arising from the shape model uncertainties (Nimmo et al., 2011; Tajeddine et al., 2017), $\sigma_{lm}^{\rm topo}$. The two are related, neglecting the effects of compensation, via Eqs. (8) and (1), as follows

$$\sigma_{lm}^{\rm topo*} = \left(\frac{3\rho_{\rm shell}}{R\bar{\rho}(2l+1)}\right)\sigma_{lm}^{\rm topo}. \tag{25}$$

Similarly, for the libration amplitude, the shaded purple bands in Figs. 3 and 4 are the combined uncertainties, given by

$$\sigma_{\gamma} = \sqrt{\sigma_{\gamma,\rm obs}^2 + \sigma_{\gamma,\rm model}^2} \tag{26}$$

where $\sigma_{\gamma,\ \rm obs} = 0.014^\circ$ (Thomas et al., 2016) and where $\sigma_{\gamma,\ \rm model}$ arises from the shape model uncertainties described above, with values of $\sigma_{\gamma,\ \rm model} = 0.004^\circ$ and $\sigma_{\gamma,\ \rm model} = 0.00025^\circ$ for the shape models of Nimmo et al. (2011) and Tajeddine et al. (2017), respectively.

2.7. Radiative equilibrium surface temperature

To compute the equilibrium surface temperature of Enceladus as a function of latitude, we take an approach similar to that of Ojakangas and Stevenson (1989) for Europa. Some differences include the fact that we cannot assume a small angle for the inclination (solar obliquity) because, whereas the Jupiter system is inclined by just ~3.13° with respect to its orbital plane, the Saturn system's inclination is ~26.73°. Also, rather than dividing the problem into its Arctic and non-Arctic parts, making appropriate approximations, and solving analytically, we simply carry out the full calculation numerically.

Consider a point, P, on the surface of Enceladus at colatitude θ. In an inertial frame centered on Enceladus with the z-axis coinciding with the spin vector, we have a unit vector pointed towards P and another unit vector pointed towards the sun. The angle, ψ, between the two vectors is given by

$$\cos\psi = \sin\theta\cdot\cos i\cdot\cos\Omega t\cdot\cos nt + \sin\theta\cdot\sin\Omega t\cdot\sin nt + \sin i\cdot\cos\theta\cdot\cos\Omega t \tag{27}$$

where i is the inclination of the Saturn system with respect to its orbital plane (and thus the solar obliquity of Enceladus given that its obliquity with respect to Saturn is not measurably different from zero), where Ω is the mean motion of Saturn's orbit around the sun, and where n is the mean motion of Enceladus in its orbit around Saturn.

The time- and latitude-dependent solar flux, $F(\theta, t)$, at a point on the surface of Enceladus is the product of the solar constant at Saturn ($F_s \approx 14.9$ W/m^2) and $\cos\psi$, and is obviously zero when $\cos\psi \le 0$, corresponding to the night side. That is

$$F(\theta, t) = \begin{cases} F_s\cos\psi & \cos\psi > 0 \\ 0 & \cos\psi \le 0 \end{cases}. \tag{28}$$

After integrating (numerically, with $dt = 1$ hr) and averaging over an entire Saturnian year ($2\pi/\Omega$), we obtain the latitude-dependent annual mean flux

$$\bar{F_A}(\theta) = \frac{\Omega}{2\pi}\int_{t=0}^{2\pi/\Omega} F(\theta, t)dt. \tag{29}$$

Finally, we compute the equilibrium surface temperature as

$$T(\theta) = \left(\frac{(1-A)\bar{F_A}(\theta)}{\sigma}\right)^{1/4} \tag{30}$$

where $A = 0.8$ is the surface albedo and $\sigma = 5.67 \times 10^{-8}$ Wm^{-2}K^{-4} is the Stefan-Boltzmann constant. The approximation proposed by Nadeau and Mcgehee (2017) delivers a nearly identical result.

2.8. Tidal dissipation, equilibrium shell thickness, and heat loss

The diurnally variable tidal stresses cause strains that dissipate heat within the ice shell. The volumetric heat dissipation, q, is a function of the assumed ice rheology and varies spatially across the body as well as with depth (due to the dependence on viscosity and thus temperature). In an equilibrium configuration, the thickness and temperature structure of the ice shell will be such that all of the heat dissipated at a given latitude and longitude will be removed radially outward by conduction (due to the much smaller temperature gradients, lateral heat flow will be negligible by comparison). That is, the surface heat flux will equal the total heat dissipated within the ice shell at a given latitude and longitude (plus any additional heat that is supplied to the shell from below). Given some surface temperature (T_s; section 2.7) and basal temperature (T_b), we wish to solve for the equilibrium shell thickness, d_{eq}.

Assuming radial outward heat conduction and using a coordinate system with z positive downward, the volumetric heat dissipation at any given point within the ice shell is also the radial gradient of the local heat flux, and can thus be related to the temperature structure as follows

$$q(T) = \frac{d}{dz}\left(-k\frac{dT}{dz}\right) = -\frac{d}{dz}\left(\frac{c}{T}\frac{dT}{dz}\right). \tag{31}$$

Here, we have expressed the thermal conductivity as a function of temperature, $k = c/T$, with $c = 651$ W/m being an experimentally derived constant (Petrenko and Whitworth, 1999, p.43). Following the approach of Ojakangas and Stevenson (1989), we can integrate this heat dissipation across the shell subject to the boundary conditions that the surface temperature is given by Eq. (30) and that the heat flux into the shell from below is H. Assuming that dissipation is a strong function of viscosity and thus temperature, such that nearly all of the dissipation is concentrated near the relatively low viscosity base of the shell, and that the gradient in $\ln T$ is approximately constant across almost the entire shell, then the laterally variable equilibrium shell thickness is given by (Ojakangas and Stevenson, 1989)

$$d_{eq}(\theta, \phi) = \frac{\ln\left(T_b/T_s(\theta, \phi)\right)}{\left(\frac{2}{c}\int_{T=0}^{T_b}\frac{q(T)dT}{T} + \left(\frac{H}{c}\right)^2\right)^{1/2}} \tag{32}$$

where θ and ϕ are the colatitude and longitude, respectively, and where the dissipation integral

$$\int_{T=0}^{T_b}\frac{q(T)dT}{T} \tag{33}$$

is a function of the assumed ice rheology. Assuming a Maxwell rheology, for example, yields (Ojakangas and Stevenson, 1989)

$$\int_{T=0}^{T_b}\frac{q(T)dT}{T} = \frac{2\mu}{nl}\bar{\xi}(\theta, \phi)\left(\frac{\pi}{2} - \tan^{-1}\left(n\frac{\eta_0}{\mu}\right)\right) \tag{34}$$

where μ is the rigidity of the ice, n is the mean motion of the satellite in its orbit (the same as its rate of spin), and η_0 is a reference viscosity corresponding to the base of the ice shell. The term $\bar{\xi}(\theta, \phi)$ is the time-averaged value of the sum of the squares of the elements of the strain rate tensor (see Ojakangas and Stevenson, 1989, Appendix B, noting the corrections by Nimmo et al. (2007)). Note that this approach assumes the dissipation takes place in a uniform thin shell. If the low viscosity part of the shell has significant variability in thickness, dissipation may be enhanced in the thinner regions (e.g., Běhounková et al., 2017; Beuthe, 2018).

The laterally varying conductive heat loss may be approximated by

$$F_{cond}(\theta, \phi) = \frac{c}{d(\theta, \phi)}\ln\left(\frac{T_s(\theta, \phi)}{T_b}\right)\left(1 - \frac{d(\theta, \phi)}{R}\right) \tag{35}$$

where the term in parentheses is required to account for the spherical geometry. Although this equation is only strictly valid when there are no heat sources within the ice, this approximation is adequate because the dissipation is concentrated very close to the base of the shell, such that the heat flux is constant across nearly all of the ice shell.

The total tidal dissipation within Enceladus can be related to the properties of its orbit and its interior via (Peale and Cassen, 1978)

$$\dot{E} = \frac{21}{2}\left(\frac{k_2}{Q}\right)\frac{GM_S^2}{a^6}R_E^5 ne^2 \tag{36}$$

where k_2 is the degree-2 tidal potential Love number for Enceladus, describing the magnitude of the response to tidal forcing, Q is the quality factor related to how much energy is dissipated on each tidal cycle, M_S is the mass of Saturn, R_E is the radius of Enceladus, a is its semi-major axis, n is its mean motion, and e is its orbital eccentricity. See Nimmo et al. (2018) for a more thorough discussion of tidal dissipation as it relates to Enceladus.

3. Ice shell structure

3.1. Observations

The shape of Enceladus has been estimated based on analysis of limb profile measurements (Nimmo et al., 2011; Thomas, 2010) and, more recently, by additionally incorporating data from a control point network (Tajeddine et al., 2017). The latter approach differs in detail from the earlier work, in particular in the way uncertainties are calculated. Because the newer analysis incorporates additional data, one would expect somewhat smaller uncertainties. However, the degree-2 coefficient uncertainties reported by Tajeddine et al. (2017) are smaller than those of Nimmo et al. (2011) by a factor of 16–46, depending on which coefficients are compared. We regard this as an indication that the uncertainties reported by Nimmo et al. (2011) and Tajeddine et al. (2017) could have somewhat distinct physical meanings, and may not therefore be directly comparable. We proceed here using the as-published uncertainties in both shape models, but we urge caution in comparing the results, as we discuss further below.

In spite of the differences between the published shape models, it is clear that Enceladus's shape departs substantially from the expectation for a body in hydrostatic equilibrium (Fig. 1). Whereas, for a hydrostatic Enceladus, the ratio between the two major degree-2 terms should be $-H_{20}/H_{22} \approx 3.25$ (e.g., McKinnon, 2015; Tricarico, 2014), the observed ratio is 4.20 ± 0.22 or 4.09 ± 0.01, according to the shape models of Nimmo et al. (2011) and Tajeddine et al. (2017), respectively. The corresponding ratio for the geoid, computed using Eq. (2) from the measured gravitational field (Iess et al., 2014), is just 3.42 ± 0.02. While this still represents a statistically significant departure from hydrostatic equilibrium, it is much closer to the hydrostatic expectation (dashed line in Fig. 1), immediately suggesting that the non-hydrostatic topography is largely compensated.

Because of the departure from hydrostatic equilibrium, we cannot obtain the moment of inertia directly. Instead, we must treat Enceladus as a mostly hydrostatic body (corresponding to some point on the hydrostatic line in Fig. 1) superimposed with some non-hydrostatic topography and its corresponding non-hydrostatic gravity. Finding a solution that satisfies the observational constraints, while handling compensation self-consistently, requires some exploration of parameter space.

To illustrate the way in which the different observations constrain the interior structure, we use shaded bands (in Figs. 2, 3, 4, 6, and 8) to show the parts of the parameter space that satisfy each observation within their uncertainties (see section 2.6). Table 1 shows, for the important gravity coefficients (C_{20}, C_{22}, C_{30}), the relative contributions to the overall uncertainty from the separate uncertainties in the gravity and shape models.

3.2. Parameter space exploration

Here, starting from the observed shape, we consider a range of possible interior models in terms of the number of layers, layer thicknesses, layer densities, and compensation mechanisms. For each model, we compute the corresponding gravitational potential using Eq. (8) and compare the result to the observed values (Iess et al., 2014), as described in section 2.6.

3.2.1. Two-layer model

For our two-layer model (core and shell), there are only two free parameters: the density and mean thickness of the ice shell. Having fixed these two values, the density and mean radius of the core are constrained by the known total radius and bulk density. We set the core shape to a hydrostatic equilibrium figure (section 2.2) and we set the exterior to match the observed shape (Nimmo et al., 2011 or Tajeddine et al., 2017). We then vary the two free parameters over a considerable range, computing the resulting gravity coefficients for each model using Eq. (8). Fig. 2 illustrates the ranges of model parameters that yield gravitational fields that match the observed J_2 (blue), C_{22} (red), or J_3 (gold) dimensionless gravitational potential coefficients (Iess et al., 2014). We compute the libration amplitude, via Eq. (17), across this parameter space but its maximum value is $\sim 0.04^{\circ}$, more than 5σ below the observed value of $0.120 \pm 0.014^{\circ}$. Only models with ice shell densities below ~ 600 kg/m^3 can simultaneously satisfy the observed J_2 and C_{22} within their 1σ bounds, though there is considerable agreement within their 2σ bounds. To satisfy the observed J_3, however, requires unreasonably small ice shell densities. The magnitude of the J_3 gravity term, obtained via Eq. (8), and resulting mainly from the large topographic depression at the south pole, is generally far too large (e.g., for $\rho_{\text{shell}} = 900$ kg/m^3, $J_3^{\text{model}} \approx -375 \times 10^{-6}$, nearly 10σ from the observed value). Hence, for reasonable ice shell densities, and independent of any other assumptions regarding the interior structure, it is clear that substantial compensation is required. Next, we explore three-layer models that allow for compensation in either the Airy sense (lateral thickness variations in a shell overlying a weaker layer) or the Pratt sense (lateral density variations in the outermost portion of the body).

3.2.2. Three-layer model with Airy compensation—sensitivity to methods

For our three-layer Airy isostatic model, there are four free parameters: the density and mean thickness of the ice shell, and the density and mean thickness of the underlying lower viscosity layer (which we call the ocean); the core radius and density are derived from the known total radius and bulk density. Although this parameter space has four dimensions, we will begin here by fixing the ice shell and ocean densities, reducing the number of free parameters to two.

The results of this type of analysis are sensitive to certain methodological choices including the way the hydrostatic equilibrium figure is computed, the way isostatic support is modeled, and whether or not the finite amplitude of the topography is taken into account. We illustrate the effects of these choices by comparing our results against results obtained under different assumptions and in previous work. Fig. 3a, for instance, follows the assumptions of Iess et al. (2014) in which the equilibrium figure is computed according to Eq. (11), placing it on the dotted line in Fig. 1. Although Fig. 3a does not resemble any figure in Iess et al. (2014), the information is essentially the same, with the exceptions that we have re-referenced the gravitational potential coefficients to a radius of 252.1 km and, for the sake of uniformity across the panels of Fig. 3, we assume here that $\rho_{\text{shell}} = 925$ kg/m^3 and $\rho_{\text{ocean}} = 1020$ kg/m^3. As discussed by McKinnon (2015), Enceladus's fast rotation causes its equilibrium figure to depart slightly from the

Table 2
Preferred interior model parameters assuming Airy compensation, with the ice shell supported buoyantly in a subsurface ocean. The table shows the results for the nominal densities (corresponding to Fig. 4) as well as the results emerging from the four-dimensional parameter space exploration (corresponding to Fig. S1), in which the layer densities were allowed to vary. Since the ice shell and ocean densities could not be constrained in that case, we show the full ranges considered and designate them with an asterisk (*). For all other parameters, the reported ranges correspond to the 68% confidence ranges emerging from the parameter space exploration. For the ice shell thicknesses, we also show the thickness found at the south pole (SP). The minimum misfit ($L_{\min}$) across the parameter space is also given for each case (see section 2.6).

		2D grid with nominal densities		4D grid with density ranges	
Shape model	Layer	Mean thickness	Density	Mean thickness	Density
Nimmo et al. (2011)	Ice shell	21 – 25 km (0 – 3 km at SP)	925 kg/m^3	19 – 24 km (4 – 12 km at SP)	*850 – 950 kg/m^3
	Ocean	37 – 44 km	1020 kg/m^3	37 – 48 km	*1000 – 1100 kg/m^3
	Core	185 – 192 km	2420 – 2590 kg/m^3	184 – 193 km	2390 – 2570 kg/m^3
		$L_{\min} = 1.6$		$L_{\min} = 0.6$	
Tajeddine et al. (2017)	Ice shell	19 – 24 km (7 – 11 km at SP)	925 kg/m^3	21 – 26 km (9 – 17 km at SP)	*850 – 950 kg/m^3
	Ocean	35 – 39 km	1020 kg/m^3	30 – 39 km	*1000 – 1100 kg/m^3
	Core	192 – 195 km	2340 – 2410 kg/m^3	191 – 198 km	2320 – 2410 kg/m^3
		$L_{\min} = 3.7$		$L_{\min} = 3.2$	

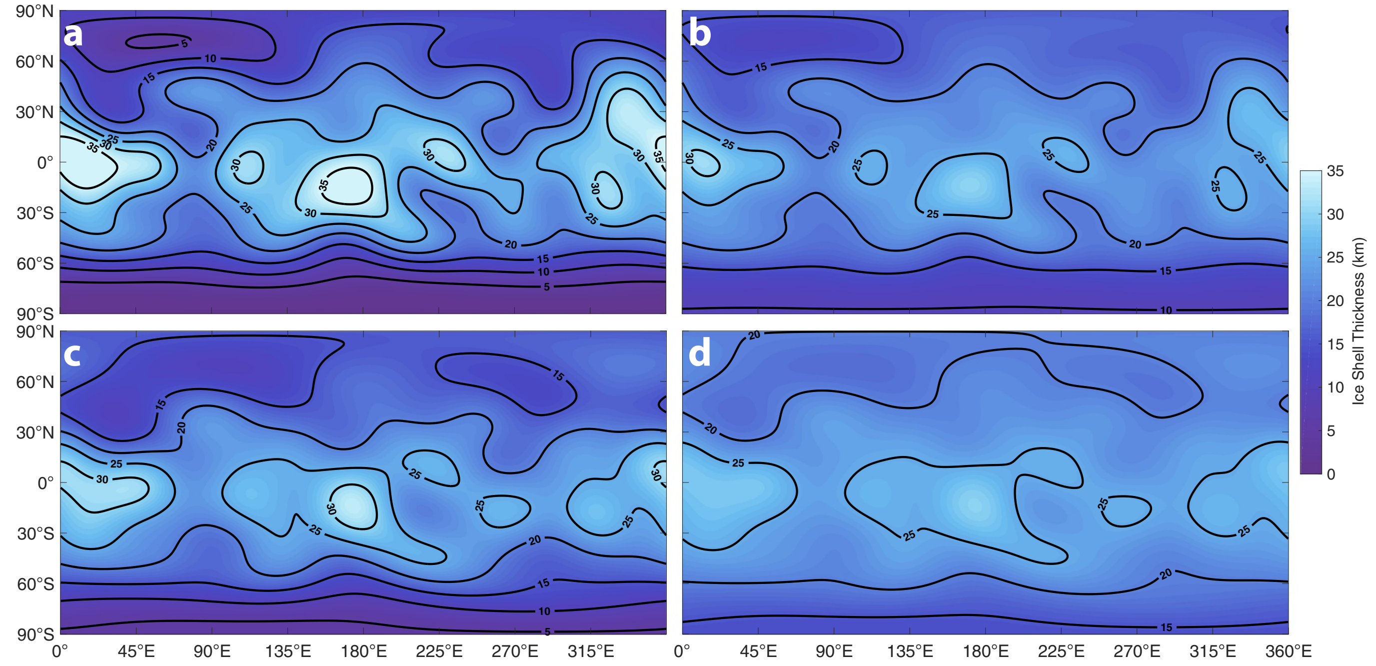

Fig. 5. Lateral shell thickness variations implied by Airy compensation assuming the topography is supported isostatically. Representative examples are shown based on the shape models of (a,b) Nimmo et al. (2011) and (c,d) Tajeddine et al. (2017), where both expansions are limited to spherical harmonic degree 8. Left panels (a,c) correspond to the nominal densities of $\rho_{\text{shell}} = 925$ kg/m^3 and $\rho_{\text{ocean}} = 1020$ kg/m^3 whereas right panels (b,d) correspond to a larger density contrast, with $\rho_{\text{shell}} = 900$ kg/m^3 and $\rho_{\text{ocean}} = 1100$ kg/m^3, thus yielding more subtle shell thickness variations. The mean layer thicknesses are chosen to give the best fit for each combination of shape model and layer densities. The mean layer thicknesses (shell/ocean/core), in kilometers, and misfits [in square brackets], are: (a) 22/42/188 [1.6], (b) 21/46/185 [0.6], (c) 21/37/194 [3.7], (d) 23/38/191 [3.2].

usual approximation—whereas it is usually assumed that $H_{20}^{\text{hyd}}/H_{22}^{\text{hyd}} = -10/3$, the appropriate value for Enceladus is ≈ -3.25. The latter value is obtained following the approach of Tricarico (2014). Although the difference in this ratio is only ~2.5%, the effect is a significant change to the point at which the J_2 (blue) and C_{22} (red) curves intersect—at a shell thickness of ~49 km rather than ~33 km, when the Nimmo et al. (2011) shape model is adopted (Fig. 3b). Once again, our illustration does not resemble any figure in McKinnon (2015), but the calculations are the same, except for the assumed layer densities, the effects of which are subtle. Figs. 3e and f show the corresponding results when the Tajeddine et al. (2017) shape model is adopted instead.

Unlike the work of Iess et al. (2014) and McKinnon, (2015), our current approach involves computing the hydrostatic equilibrium figures for all three layers (section 2.2). The hydrostatic equilibrium figure is then maintained for the core (a topic we return to in section 3.2.6) while the shape of the outermost surface is set to match the observations (Nimmo et al., 2011 or Tajeddine et al., 2017), and the shape of the ice/ocean interface is set to ensure that the topography is supported via Airy isostatic compensation. Also unlike Iess et al., (2014) and McKinnon, (2015), which effectively treat the topography as surface density anomalies for purposes of computing the resulting gravitational field, our current approach includes a correction accounting for the finite amplitude of the topography (Wieczorek and Phillips, 1998). Fig. 3c illustrates the results obtained when we compute the equilibrium figures using the numerical approach of Tricarico (2014) and when we apply the finite amplitude correction (Wieczorek and Phillips, 1998).

Both Iess et al. (2014) and McKinnon (2015) followed what we call the "equal masses" approach to isostasy (e.g., Lambeck, 1988) in which columns of equal width are required to contain equal masses. As discussed by Hemingway and Matsuyama, (2017), however, this does not eliminate lateral pressure gradients at depth, and therefore may not correspond to an equilibrium condition (see also Beuthe et al., 2016). Whereas the "equal masses" approach to isostasy was maintained for Fig. 3c, we instead advocate the "equal pressures" approach to isostasy (Hemingway and Matsuyama, 2017), wherein the goal is to eliminate lateral pressure gradients at depth (see discussion in section 2.3). The effect is dramatic (Fig. 3d), with the J_2 (blue) and C_{22} (red) curves now intersecting at a shell thickness of ~30 km, when the Nimmo et al. (2011) shape model is adopted. Moreover, whereas the J_3 (gold) curve was not sensitive to the way in which the equilibrium figure was computed (compare Fig. 3a and b), it is strongly affected by the change in the approach to isostasy, shifting from a preferred shell thickness of more than 40 km (Fig. 3c, "equal masses") to just ~20 km (Fig. 3d, "equal pressures"). Figs. 3g and h illustrate the corresponding results when the Tajeddine et al. (2017) shape model is adopted instead. Fig. 3c, d, g, and h additionally illustrate the parts of the parameter space that best satisfy the observed libration amplitude (purple line), demonstrating that the libration constraint agrees best with the gravity constraints when the "equal pressures" model is adopted, consistent with the results of Beuthe et al. (2016). This is also evident from the minimum misfit values provided in the caption. From here on, our results employ the "equal pressures" isostasy model exclusively.

3.2.3. *Three-layer model with Airy compensation—results*

Fig. 4 shows, for one example combination of ice shell and ocean densities ($\rho_{\text{shell}} = 925$ kg/m^3 and $\rho_{\text{ocean}} = 1020$ kg/m^3), the ranges of shell and ocean thicknesses that yield, via Eq. (8), gravitational fields that match the observed J_2 (blue), C_{22} (red), or J_3 (gold) (Iess et al., 2014), as well as those thicknesses that yield, via Eq. (20), a libration amplitude that matches the observed value (purple). This two-dimensional slice of the parameter space serves to illustrate how the model gravitational potential coefficients and libration amplitude vary as a function of shell and ocean thickness. All three gravity coefficients are sensitive to the assumed shell thickness because this determines how effectively the isostatic compensation reduces the magnitude of the non-hydrostatic gravity arising from the non-hydrostatic topography.

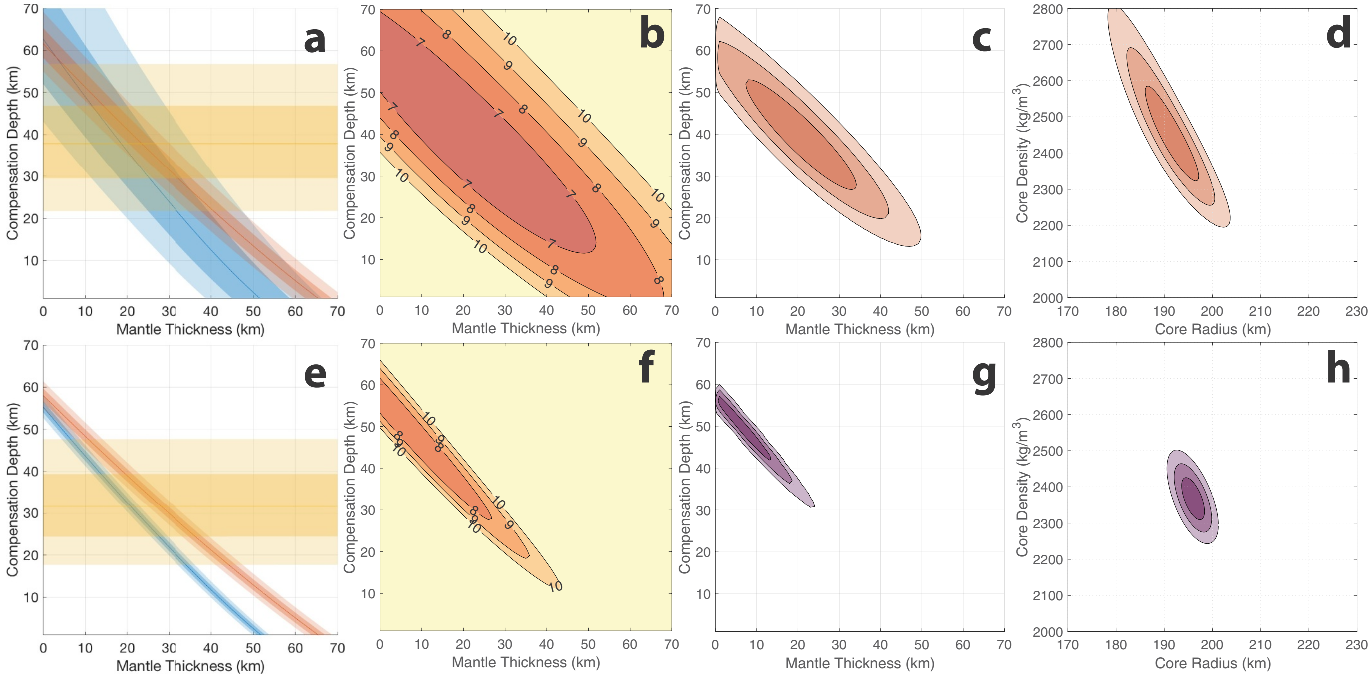

Fig. 6. Misfits and probability densities across the parameter space assuming a three-layer model with Pratt compensation, assuming mean densities ρ_{shell} = 925 kg/m^3 and ρ_{mantle} = 1030 kg/m^3, and comparing results derived from the shape models of (a–d) Nimmo et al. (2011) and (e–h) Tajeddine et al. (2017). (a,e) Lines indicate combinations of compensation depth and mantle thickness that satisfy the observed J_2 (blue), C_{22} (red), or J_3 (gold) dimensionless gravitational potential coefficients (Iess et al., 2014), with shaded bands indicating 1σ (dark) and 2σ (pale) bounds from combined shape and gravity model uncertainties (section 2.6). (b,f) Misfit between the model and the observations, given by Eq. (21). (c,g) 68% (dark), 95% (intermediate), and 99.7% (pale) confidence contours showing compensation depths and mantle thicknesses that best account for the observed gravitational potential, and (d,h) corresponding core radius and density (section 2.6). The minimum misfits are L = 6.0 and L = 7.0 for the Nimmo et al. (2011) and Tajeddine et al. (2017) shape models, respectively. (For interpretation of the references to color in this figure legend, the reader is referred to the web version of this article.)

Only the two degree-2 coefficients, however, are also sensitive to the assumed ocean thickness. This is because the magnitude of the hydrostatic component of those coefficients depends on the overall radial density structure of the body. Since there is no hydrostatic component to the J_3 term, it is not sensitive to ocean thickness, except insofar as the hydrostatic components affect the total amplitude of the topography, thereby affecting the potential via the finite amplitude correction (Wieczorek and Phillips, 1998). Similarly, the libration amplitude is mainly sensitive to the mean shell thickness because this directly determines the shell's moment of inertia (C_s). The libration amplitude is also weakly sensitive to the mean ocean thickness because this slightly alters the moment of inertia of the core and also affects the decoupled system's natural frequencies as well as the torques acting on the different parts of the system (section 2.5). Because the libration amplitude is an inverse function of shell thickness, it increases rapidly at small shell thicknesses, effectively providing a strong lower bound on shell thickness—this is evident in the shapes of the misfit contours in Fig. 4b and f.

The misfits are larger when the Tajeddine et al. (2017) shape model is adopted instead of that of Nimmo et al. (2011), primarily because of the much smaller uncertainties. As we discussed in section 3.1, however, the two studies took very different approaches in their analyses of uncertainties such that the two results may not be directly comparable. In principle, the minimum misfit of L = 3.7 (Fig. 4f) can be interpreted as an indication that there are no points in the parameter space that simultaneously satisfy all of the observations within their 1σ uncertainties and that additional model parameters may be required to accommodate the observations. Although we do explore additional model parameters below (sections 3.2.5 and 3.2.6), we emphasize that the meaning of the uncertainties reported by Tajeddine et al. (2017) is not entirely clear and should perhaps be interpreted with caution. As discussed in section 2.6, since we cannot evaluate the likelihood of any particular model in absolute terms, we instead focus on the shapes of the probability density functions to indicate, within the context of each model, which model parameters fit best (e.g., Fig. 4c, d, g, and h).

Whereas Fig. 4 illustrates only a two dimensional slice of the parameter space, with a fixed combination of shell and ocean densities, we consider a wide range of possible densities for both the shell and the ocean, leading to a four dimensional parameter space. We compute the misfit and use it to compute the probability density everywhere across this four dimensional parameter space (section 2.6), subject to the constraint that the shell and ocean thicknesses must be everywhere greater than zero. Fig. S1 shows confidence contours illustrating the ranges of model parameters that best account for the observed gravitational potential and libration amplitude. The preferred shell thickness is not sensitive to the assumed densities for the ice shell and ocean, though slightly better fits tend to occur for smaller ice shell densities and larger ocean densities. The preferred ocean thickness also increases slightly with both ice shell density and ocean density, but neither of these densities are well constrained. Though there is considerable overlap between the confidence contours arising from the two different shape models, the newer shape model (Tajeddine et al., 2017) tends to favor slightly larger ice shell thicknesses and smaller ocean thicknesses (Table 2).

Although Figs. 4 and S1 refer only to the mean shell thickness, Airy compensation entails considerable lateral shell thickness variations. Fig. 5 illustrates, for four example interior models, the lateral shell thickness variations assuming that all of the topography is supported by Airy isostasy. The four cases correspond to the best fitting interior models for each shape model given two different sets of layer densities (a nominal reference set of densities and a high density contrast case). The amplitude of the shell thickness variations is a function, via Eq. (12), of the density contrast between the ice shell and the ocean, with larger density contrasts corresponding to subtler shell thickness variations (Fig. 5b and d). The shell is always thinnest at the poles and

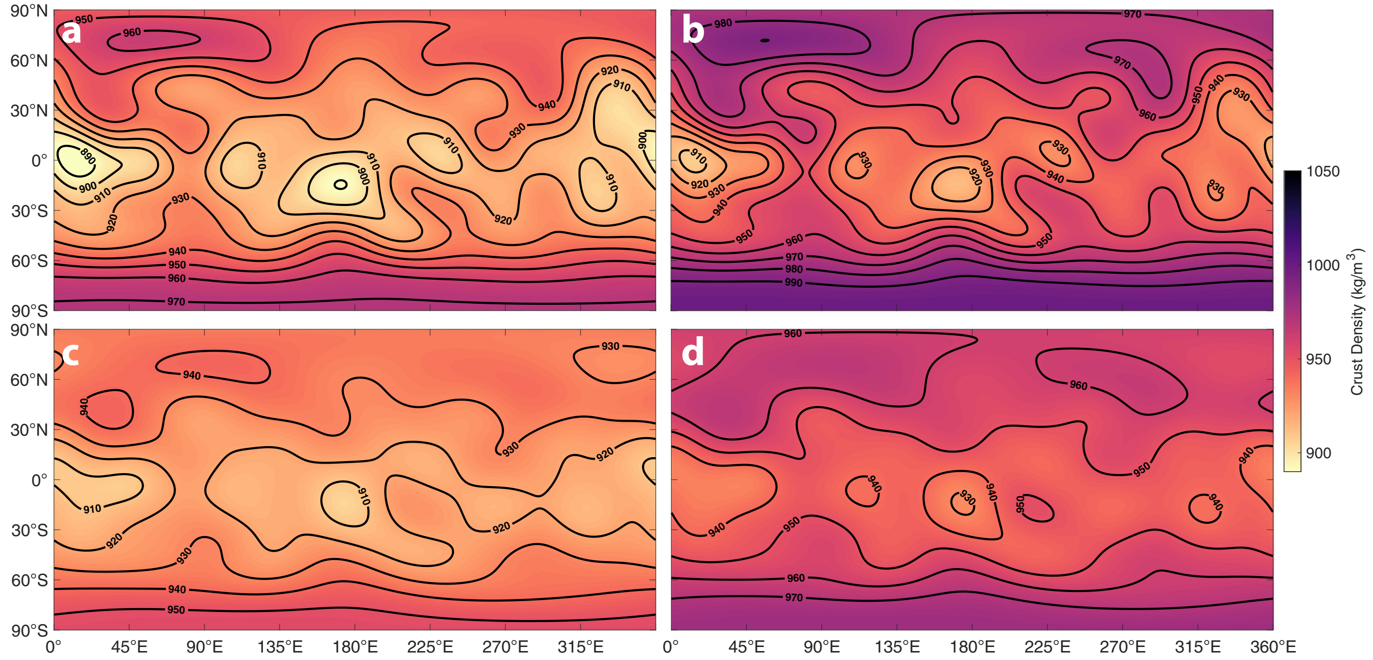

Fig. 7. Lateral shell density variations implied by Pratt compensation assuming all of the model topography is supported isostatically. Representative examples are shown based on the shape models of (a,b) Nimmo et al. (2011) and (c,d) Tajeddine et al. (2017). Left panels (a,c) correspond to the nominal densities of ρ_{shell} = 925 kg/m^3 and ρ_{mantle} = 1030 kg/m^3 whereas right panels (b,d) correspond to larger densities, with ρ_{shell} = 950 kg/m^3 and ρ_{mantle} = 1300 kg/m^3. The approximate mean layer thicknesses (shell/mantle/core), in kilometers, and misfits [in square brackets], are: (a) 39/21/192 [6.0], (b) 38/35/179 [6.0], (c) 49/7/196 [7.0], (d) 49/13/190 [7.0].

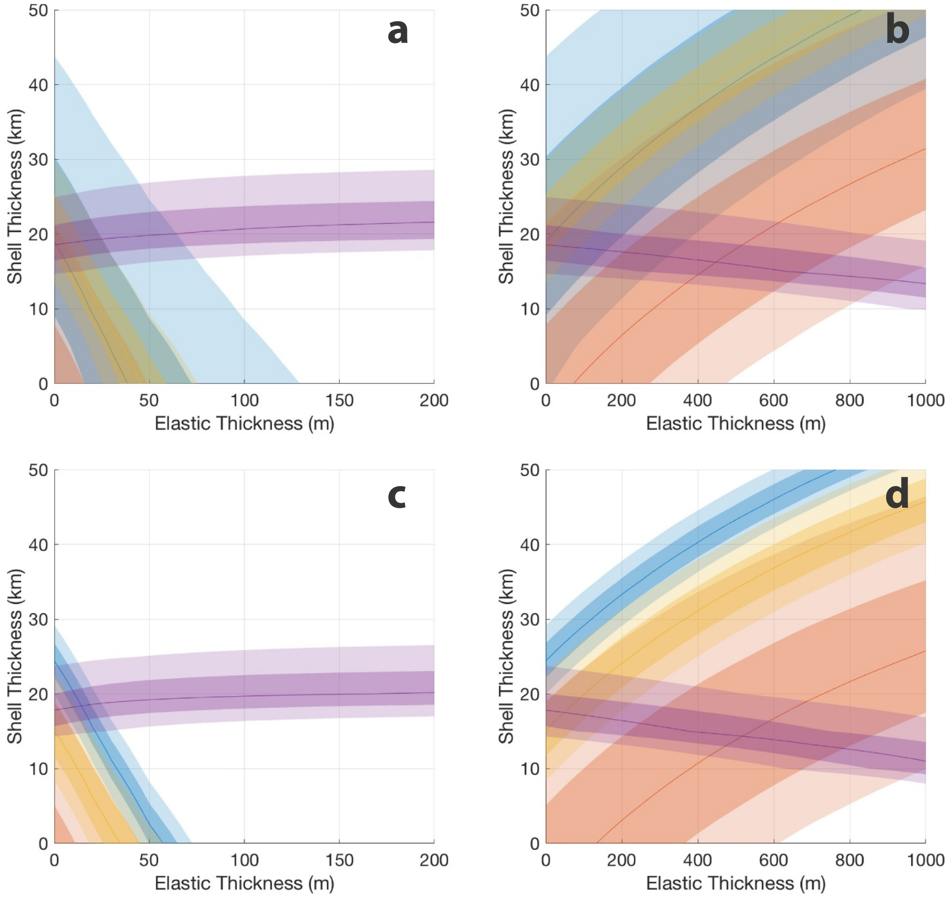

Fig. 8. Effect of elastic flexural support on the best fitting shell thickness under the assumption of either (a,c) top loading; or (b,d) bottom loading, and adopting the shape models of (a,b) Nimmo et al. (2011) or (c,d) Tajeddine et al. (2017). Lines indicate combinations of ice shell thickness (i.e., compensation depth) and elastic layer thicknesses (T_e) that satisfy the observed J_2 (blue), C_{22} (red), or J_3 (gold) dimensionless gravitational potential coefficients (Iess et al., 2014), and the observed libration amplitude (purple) (Thomas et al., 2016), with shaded bands indicating 1σ (dark) and 2σ (pale) uncertainties on the estimated values (section 2.6). The minimum misfits are: (a) L = 1.9, (b) L = 1.9, (c) L = 3.4, and (d) L = 3.7. (For interpretation of the references to color in this figure legend, the reader is referred to the web version of this article.)

thickest at the equator, especially near the prime- and anti-meridians. The thinnest parts of the shell correspond to the topographic depressions near the poles, with the thinnest part of the shell coinciding with the South Polar Terrain (SPT). We emphasize that, although we show only four examples in Fig. 5, a range of interior models and shell thicknesses are compatible with the observational constraints (Fig. S1, Table 2).

3.2.4. Three-layer model with Pratt compensation

For our three-layer Pratt isostatic model, there are four free parameters: the mean densities and thicknesses of the two outer layers; the core radius and density are derived from the known total radius and bulk density. We assume the outermost layer is composed of water ice with a nominal mean density of 925 kg/m^3 (though we consider a range between 850 and 950 kg/m^3). Pratt compensation is accomplished through relatively smaller lateral density variations in this outer layer. We refer to the mean thickness of the outer layer as the compensation depth, since the compensating density anomalies occur throughout this layer. We refer to the intermediate layer between the ice shell and the core as the mantle and we assume it is part of the primarily water ice envelope surrounding the core, and hence its density is only slightly higher than that of the overlying ice shell (we consider mantle densities in the range of $1000 - 1300$ kg/m^3). As with the Airy model, we begin by computing the hydrostatic equilibrium figures for all layers (section 2.2). The hydrostatic equilibrium figure is then maintained for the core (see section 3.2.6) while the shape of the outermost surface is set to match the observations (section 3.1). Finally, the required lateral density anomalies, computed via Eq. (13), are applied to the outer layer in order to achieve Pratt isostatic compensation (section 2.3; Hemingway and Matsuyama, 2017).

Fig. 6 shows, for one example combination of mean shell and mantle densities ($\rho_{\text{shell}} = 925$ kg/m^3 and $\rho_{\text{mantle}} = 1030$ kg/m^3), the ranges of shell and mantle thicknesses that yield, via Eq. (8), gravity fields that match the observed J_2 (blue), C_{22} (red), or J_3 (gold) (Iess et al., 2014). This two-dimensional slice of the parameter space serves to illustrate how the model gravitational potential coefficients vary as a function of compensation depth and mantle thickness. As with the Airy compensation case, all three coefficients are sensitive to the assumed compensation depth because this determines how effectively the isostatic compensation reduces the magnitude of the non-hydrostatic gravity arising from the non-hydrostatic topography. Only the two degree-2 coefficients, however, are also sensitive to the assumed mantle thickness. This is because the magnitude of the hydrostatic component of those coefficients depends on the overall radial density structure of the body. As with the two-layer model, for the three-layer Pratt model, where it assumed that the layers are physically coupled (cannot easily slide against each other), the maximum libration amplitude, computed via Eq. (17), is $\sim 0.04^{\circ}$, more than 5σ below the observed value of $0.120 \pm 0.014^{\circ}$, meaning that no part of this parameter space is compatible with the observed libration amplitude (Thomas et al., 2016). Consideration of the Pratt model nevertheless remains useful for determining the compensation depth that would be required to accommodate the gravity observations; in principle, a thin decoupling liquid layer could be inserted between the mantle and core, permitting a larger libration amplitude.

Whereas Fig. 6 illustrates only a two dimensional slice of the parameter space, with a fixed combination of shell and mantle densities, we consider a wide range of possible densities for both the shell and the mantle, leading to a four dimensional parameter space. We compute the misfit and use it to compute the probability density everywhere across this four dimensional parameter space (section 2.6), subject to the constraint that the shell and mantle thicknesses must be everywhere greater than zero. Fig. S2 shows 68%, 95%, and 99.7% confidence contours illustrating the ranges of model parameters that best account for the observed gravitational potential. The preferred shell thickness is not sensitive to the assumed mean densities for the ice shell and mantle, though slightly better fits tend to occur for larger shell and mantle densities. Owing to the relatively smaller uncertainties in the Tajeddine et al. (2017) shape model, the confidence contours enclose a much smaller part of the parameter space, with a strong preference for large shell thicknesses and small mantle thicknesses.

So far, we have discussed only the mean density of the outer ice shell, but the Pratt compensation mechanism entails lateral variations in the ice shell density. Fig. 7 illustrates, for four example interior models, the required lateral density variations under the assumption of Pratt isostatic compensation. The four cases correspond to the best fitting interior models for each shape model given two different sets of mean layer densities (a nominal reference set of densities and the maximum density case). When the density variations occur in a 40 km thick compensating layer, Pratt compensation implies $4 - 5\%$ higher density ice in the South Polar Terrain (SPT) and in the heavily cratered region on the eastern hemisphere at high northern latitudes. When the compensating layer is only 20 km thick, the required density anomaly is $8 - 10\%$.

3.2.5. Flexural support

If part of the ice shell behaves elastically, and if the shell thickness variations were generated after the formation of this elastic layer, then, in addition to buoyant support, the topography will be supported in part by bending and membrane stresses (e.g., Turcotte et al., 1981). In such a situation, the basal topography cannot be computed with Eq. (12) and must instead be computed using Eqs. (14) or (15), depending on how the thickness variations were generated (see Appendix A). The distinction between Eqs. (14) and (15) is important. For a given observed surface relief, in the case of loading (thickening/thinning) at the surface, additional rigidity (increasing T_e and thus ζ) means relatively smaller topography at the base of the shell whereas, for basal loading, additional rigidity means relatively greater basal topography. The choice of top versus bottom loading thus drives the resulting basal topography amplitude in opposite senses, with the difference becoming increasingly significant for increasingly stiff elastic shells (Fig. 8).

The assumption of top loading was adopted in a study by Čadek et al. (2016), leading the best fitting ice shell thickness to decrease with increasing shell rigidity until it came into agreement with the results implied by the libration observations (Thomas et al., 2016). A similar situation is illustrated in Fig. 8a and c, except that, as discussed above, we are using a different approach to computing the equilibrium figures and a different approach to isostasy. However, the assumption of top loading is appropriate only if the topography arises due to surface processes such as impacts or the emplacement of erupted materials. By contrast, we regard tidal heating (and the associated asymmetries in melting and freezing at the base of the ice shell) as the dominant source of long wavelength shell thickness variations. That is, we regard bottom loading as the more appropriate model for the generation of long wavelength shell thickness variations on Enceladus. Accordingly, increasing elastic thickness translates to relatively larger basal topography and therefore requires larger mean shell thicknesses in order to satisfy the observed gravity (Fig. 8b and d) (see also Beuthe et al., 2016, Text S7).

For Fig. 8, in order to clearly illustrate how the non-hydrostatic parts of the gravitational field depend on the compensation depth (i.e., shell thickness) and the elastic layer thickness, we fixed the moment of inertia factor to an arbitrary value of 0.335, therefore maintaining a fixed hydrostatic component across this parameter space. Because lines of constant moment of inertia factor are nearly parallel to lines of constant C_{22} in Fig. 4a and e, C_{22} varies only slightly across the parameter space illustrated in Fig. 8. Hence, the C_{22} gravity observation does not provide a strong constraint on the elastic layer thickness, as illustrated by the broad red shaded bands in Fig. 8. Due to the large uncertainties in the Nimmo et al. (2011) shape model, the J_2 term is similarly of limited usefulness. The J_3 term is more useful, as illustrated by the relatively smaller gold bands in Fig. 8. Finally, the observed libration amplitude provides an independent constraint that agrees best with the gravity constraints when the elastic thickness is near zero (at the left edge of the parameter space). The libration amplitude depends weakly on the elastic layer thickness, mainly because of the effect on the shape of the ice/ocean interface. We do not take into consideration any dynamical effects that the elasticity of the ice shell might have on the libration amplitude, and we do not expect such effects to be significant for Enceladus (see section 2.5; Van Hoolst et al., 2016).

We also carried out a three dimensional parameter space exploration, varying shell and ocean thickness as well as elastic layer thickness, while keeping the shell and ocean densities fixed at their nominal values of $\rho_{\text{shell}} = 925$ kg/m^3 and $\rho_{\text{ocean}} = 1020$ kg/m^3. We did this for both the top- and bottom-loading cases (Figs. S3 and S4). The three dimensional parameter space exploration demonstrates that the best fitting ice shell thickness increases with increasing elastic thickness when bottom loading is assumed, and decreases with increasing elastic thickness when top loading is assumed, consistent with the discussion above and in Appendix A. In any case, the best fits always correspond to an elastic layer thickness ≤ 20 m—that is, simultaneously accommodating the gravity and libration observations becomes increasingly difficult with increasing elastic layer thickness (Figs. S3 and S4). We conclude from this that elastic support must not be effective for the longest wavelength topography on Enceladus. This conclusion is perhaps not surprising given the heavily fractured south polar region, where long wavelength bending and membrane stresses may be interrupted (e.g., Soucek et al., 2016; Beuthe et al., 2016). This is not to say the elastic thickness must be everywhere negligible, as the cold upper part of the ice shell should behave elastically in regions where it is not too heavily fractured. But even on local scales, for example, the effective elastic layer thickness has been estimated at just ~ 0.3 km based on apparent plate flexure at a rift zone (Giese et al., 2008) or $0.4 - 1.4$ km based on a series of ridges and troughs under an unstable extension model (Bland et al., 2007).

3.2.6. *Core topography*

Our analysis has assumed that the shape of the core corresponds to the expectation for hydrostatic equilibrium. If the core is weak (e.g., Roberts, 2015), as expected if it consists of fluid-saturated unconsolidated materials (i.e., a mud-like core), or even if it is presently strong but was weak for an extended period early in its history, it may be reasonable to expect the core to conform to a hydrostatic equilibrium figure. If, however, the core exhibits sufficient strength to maintain a departure from the expected hydrostatic equilibrium figure, then this non-hydrostatic core topography will contribute to the observed gravitational field (e.g., McKinnon, 2013; Tajeddine et al., 2014). And because of the relatively large density contrast between the core and the overlying water/ice, a significant contribution can be made with relatively little core topography.

While it is always possible to arrange such unseen core topography so as to aid in reducing the observed non-hydrostatic gravity coefficients (i.e., compensating for the non-hydrostatic topography), there is no physical reason to expect it to be so arranged—effectively mirroring the long wavelength non-hydrostatic topography in the same way that isostatic roots would, resulting in a reduction in the non-hydrostatic part of J_2. If anything, core topography might be expected to make a positive contribution to the non-hydrostatic part of J_2 since Enceladus was likely spinning even faster (experiencing greater centrifugal flattening) earlier in its history when the core was forming. Since both the magnitude and sign of any non-hydrostatic core topography are unknown, we adopt the simplest assumption, which is that the core shape matches the expectation for hydrostatic equilibrium. In principle, the unknown core topography could be taken into account using additional dimensions in the parameter space, with some *a priori* assumptions about the reasonable range of possibilities. Doing so would have the effect of widening the probability density functions shown above, but should not bias the best fitting results one way or another.

Nevertheless, in order to provide a sense of what core topography would be required to achieve a perfect match to the observed gravitational field, we solved Eq. (8) for the required core topography given the observed gravity (Iess et al., 2014), setting aside the finite amplitude correction for simplicity. When there is no isostatic compensation, some 1500 m of non-hydrostatic core topography is required (Fig. S5a) to accommodate the observed gravity. When the topography is supported by Airy compensation as in section 3.2.3, where the smallness of the non-hydrostatic gravity is explained mainly by isostatic compensation, then just ~ 350 m of non-hydrostatic core topography is sufficient (Fig. S5b) to accommodate the small remaining non-hydrostatic gravity.

3.3. *Summary*

The above parameter space exploration demonstrates that, in order to accommodate the observed shape and gravity, significant compensation is required (section 3.2.1). In principle, the observations could be accommodated by either Airy or Pratt compensation (sections 3.2.3 and 3.2.4, respectively), but the Airy model is preferred for several reasons. First, the large amplitude of Enceladus's forced physical librations (Thomas et al., 2016) implies a global subsurface ocean, which implies a floating ice shell. A floating ice shell is likely to experience laterally variable tidal dissipation (see section 4), naturally leading to lateral shell thickness variations and therefore at least some degree of Airy compensation. The presence of a decoupling ocean in the Airy models also permits large libration amplitudes and is one of the main reasons the misfits are much smaller in the Airy models (Fig. 4) than in the others (Figs. 2 and 6).

Second, even if Pratt isostasy were to dominate within the floating ice shell, it would require the systematic lateral density variations to be distributed through a layer that is some $40 - 60$ km thick (Fig. 6g) when the Tajeddine et al. (2017) shape model is adopted, or $20 - 60$ km thick (Fig. 6c) when the Nimmo et al. (2011) shape model is adopted. The libration amplitude, however, implies an ice shell thickness of roughly $16 - 22$ km, depending on the ocean thickness and assumed layer densities (Fig. 4a, e; *cf.* Thomas et al., 2016; Van Hoolst et al., 2016). Whereas this range is marginally compatible with the gravity results when the older shape model (Nimmo et al., 2011) is adopted, the newer shape model (Tajeddine et al., 2017) leads to a result that requires an ice shell roughly twice as thick as that implied by the libration amplitude.

Third, although the amplitude of the Pratt-required systematic lateral density variations is modest, and could in principle be accounted for by variations in porosity (Besserer et al., 2013), the spatial pattern (Fig. 7) is only partially consistent with the geological constraints (e.g., Crow-Willard and Pappalardo, 2015). Specifically, the Pratt mechanism requires relatively higher densities in the south polar region as well as at high northern latitudes on the trailing hemisphere. Whereas the geologically active south polar region is characterized by a youthful surface and may well have experienced thermally driven compaction (Besserer et al., 2013), the high northern latitudes are instead characterized by an ancient and heavily cratered surface with no signs of anomalous heating or porosity reduction that could lead to a positive density anomaly. This is not to say that lateral density variations do not exist. Indeed, compaction may be the best way to account for some of the large (but not global) scale topographic basins (e.g., those discussed by Nimmo et al., 2011; Schenk and McKinnon, 2009; Tajeddine et al., 2017). Some hybrid of Airy and Pratt support is of course possible at the longest length scales as well. However, it is clear that the Pratt mechanism cannot dominate.

For our Airy compensation model, the primary parameters are the ice shell and ocean thicknesses while the core radius and density are derived parameters. We assume a hydrostatic figure for the core because, although contributions from core topography cannot be ruled out, they are not expected to bias the results one way or the other (section 3.2.6). We additionally take the ice shell and ocean densities to be free parameters, but their effects are so subtle that they cannot be meaningfully constrained by shape, gravity, and libration observations alone (Fig. S1). The dominant terms of the quadrupole gravity field, J_2 and C_{22}, effectively constrain the thickness of the H_2O envelope, and therefore the core radius and density, but allow for trade-offs in how this envelope is partitioned into its solid and liquid components (Fig. 4a, e). By contrast, the zonal part of the octopole field, J_3, is insensitive to ocean thickness and therefore better constrains ice shell thickness (Fig. 4a, e), underscoring the importance of obtaining good observational constraints on the higher order terms of the gravitational field. The libration amplitude is likewise strongly sensitive to shell thickness but is only subtly and indirectly affected by ocean thickness (Fig. 4a, e; section 2.5). Expanding the parameter space exploration to allow for a range of possible ice and ocean densities does not significantly alter the best fitting parameters. This additional parameter space does, however, permit larger density contrasts and therefore subtler shell thickness variations, allowing for larger south polar shell thicknesses (Table 2).

Assuming the long wavelength topography is primarily the result of asymmetric ocean freezing, the inclusion of an elastic layer would mute the surface expression of the lateral shell thickness variations, implying larger isostatic roots (section 3.2.5). In that case, a larger mean shell thickness would be required to accommodate the observed gravitational potential (*cf.* Čadek et al., 2016). Such models, however, lead to larger misfits compared with the observations and, in some cases, grounding of the ice shell onto the core (as the mean ocean thickness becomes too small to accommodate the considerable topography at the ice-ocean interface)—a situation that is precluded by the large physical libration amplitude. Furthermore, significant elastic support requires that large membrane stresses be transmitted across the heavily fractured South Polar Terrain (SPT), which may be difficult (Soucek et al., 2016) given that the Tiger Stripe fractures likely penetrate the ice shell completely.

Adopting a pure Airy isostasy model then, and focusing on the results based on the new shape model (Tajeddine et al., 2017), the preferred mean shell and ocean thicknesses are $19 - 24$ km and $35 - 39$ km (68% confidence ranges), respectively (Fig. 4g) and the corresponding core radius and density are $192 - 195$ km and $2340 - 2410$ kg/m^3 (68% confidence ranges) (Fig. 4h), a density suggestive of hydrated silicates and/or some degree of porosity in the core (Table 2). Importantly, the shell thickness ranges from typically ~ 35 km near the prime- and anti-meridians to as little as ~ 5 km at the south pole (Fig. 5c). We emphasize that a range of different mean shell thicknesses are permitted by the observations and that this range should be taken into consideration in any attempt to understand the evolution of the ice shell, its response to tidal stresses, and the nature of ocean to surface pathways. This is particularly important for the south polar region where the ice shell thickness could be anywhere from 4 km to 14 km (our 95% confidence range), assuming nominal ice and ocean densities and adopting the newer shape model (Tajeddine et al., 2017).

4. Internal heat production

Here we discuss what the inferred shell structure implies about the heat budget of Enceladus and how and where heat is dissipated within its interior.

4.1. Heat budget

Given the range of possible mean shell thicknesses (Table 2), we can use Eq. (35) to approximate the likely range of total conductive heat loss. If solid state convection were taking place in the ice shell, the heat loss would be much greater and maintaining significant lateral shell thickness variations would be very difficult. Given that we infer significant lateral shell thickness variations (Fig. 5), we consider global scale ice shell convection to be unlikely and we focus instead on conductive heat loss. Conductive heat loss is an inverse function of shell thickness and, focusing on the result based on the new shape model (Tajeddine et al., 2017), ranges from ~ 20 to 35 GW, where we have considered ocean temperatures in the range of 220 K to 273 K (Fig. 10). This calculation does not include the additional advective heat loss associated with the eruptions in the South Polar Terrain (SPT), which may be in the vicinity of ~ 5 GW (Howett et al., 2011; Spencer et al., 2013). Hence, within our 68% confidence range of likely mean shell thicknesses, the implied total heat loss is in the range $25 - 40$ GW.

By comparison, assuming a chondritic radiogenic heating rate of 4.5×10^{-12} W/kg (Spohn and Schubert, 2003) and a chondritic mass fraction of ~ 0.5 (obtained by assuming the chondritic component density to be 3500 kg/m^3 while the remainder has a density of 1000 kg/m^3), radiogenic heating within the rocky core is < 0.3 GW. Tidal dissipation is potentially greater as Enceladus's eccentric orbit is maintained by its 2:1 mean motion resonance with Dione, and Saturn's abundant rotational energy is gradually transferred into the satellites. Making traditional assumptions about Saturn's dissipation quality factor ($Q \approx 18{,}000$), the long term average tidal dissipation within Enceladus is, however, limited to just ~ 1.1 GW (Meyer and Wisdom, 2007, 2008).

This significant shortage of heat supply would imply a rapidly freezing ocean (e.g., Roberts and Nimmo, 2008). However, recent astrometric observations (Lainey et al., 2012, 2017) indicate that Saturn may be effectively much more dissipative than previously thought, with a Q as small as perhaps ~ 2000, permitting the tidal dissipation within Enceladus to be as much as ~ 25 GW; if $Q < 2000$, the dissipation would be even greater still. Note that this low value of Q for Saturn may be time- and frequency-dependent, and may vary from satellite to satellite as each satellite's tidal interactions with Saturn occur on different timescales. Importantly, the resonance locking mechanism proposed by Fuller et al. (2016) permits these low effective present-day values for Q, and the corresponding large tidal dissipation rates, without requiring the satellites to be young (see Nimmo et al., 2018 for a more thorough discussion). Hence, the long-term average tidal dissipation rate within Enceladus may be comparable to the inferred conductive heat loss, permitting a balanced heat budget and an interior that is close to steady state.

4.2. Spatial pattern

If the tidal dissipation occurs mainly near the base of the ice shell, where the ice behaves viscously on a timescale comparable to the orbital period of 1.37 days, we can use a thin-shell tidal heating model (section 2.8) to compute the spatial pattern of tidal dissipation within the ice shell (Fig. 11a). The corresponding equilibrium ice shell structure is characterized by being thinnest at the poles and thickest at the equator, especially at the prime- and anti-meridians (Fig. 11c), in agreement with the inferred shell structure (Fig. 11d). Note that this predicted shell structure differs somewhat from that expected for Europa (e.g., Ojakangas and Stevenson, 1989) where the shell thickness is greater at the poles due to the low surface temperatures resulting from the small solar obliquity. Assuming an ocean temperature of 273 K, our model gives a mean shell thickness of 21 km (matching the inferred mean thickness) when the total dissipation is ~ 35 GW (Fig. 11b), corresponding to an interior characterized by $k_2/Q \approx 0.02$ (see section 2.8). Note that this total dissipation is a free parameter in our ice shell tidal heating model, which we tune to achieve the desired mean shell thickness (see discussion in section 4.3, below). That is, our tidal heating model does not make a prediction about the mean shell thickness, only the spatial pattern in the shell thickness variations. Nevertheless, the broad agreement between the inferred shell structure and the lateral thickness variations predicted by the ice shell tidal heating model suggests that tidal dissipation near the base of the ice shell may be an important source of internal heat production.

By contrast, assuming eccentricity tides, tidal dissipation within the

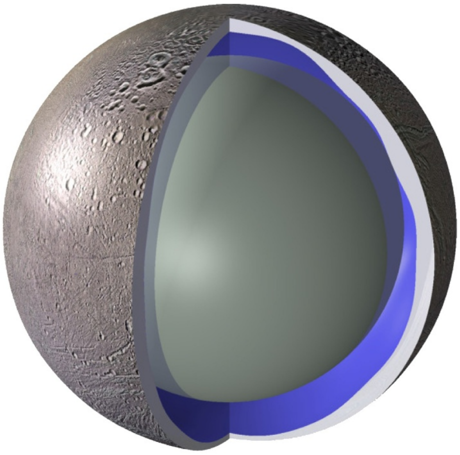

Fig. 9. Depiction of the approximate interior structure of Enceladus, to scale, assuming the topography (Tajeddine et al., 2017) is supported by complete Airy compensation (Hemingway and Matsuyama, 2017), assuming nominal densities of $\rho_{\text{shell}} = 925\ \text{kg/m}^3$ and $\rho_{\text{ocean}} = 1020\ \text{kg/m}^3$, and mean shell and ocean thicknesses of 21 km and 37 km, respectively. The ice shell and ocean are cut away between the prime meridian and 90°E. The corresponding core radius and density are approximately 194 km and $2400\ \text{kg/m}^3$. Surface texture is a global map of Enceladus produced by Paul Schenk (Lunar and Planetary Institute) from Cassini ISS data (NASA, JPL).

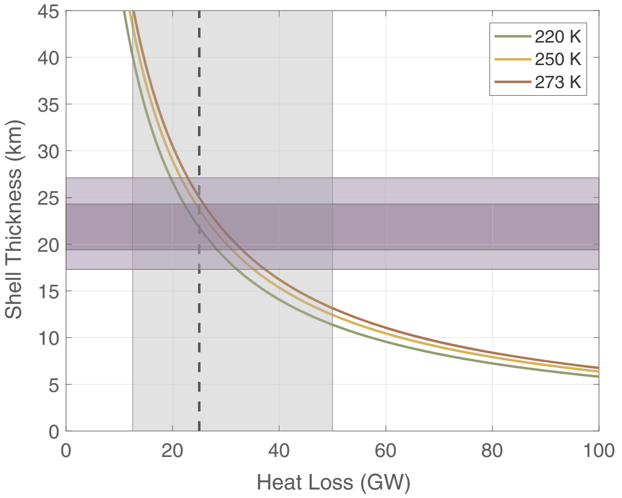

Fig. 10. Mean shell thickness versus total heat loss assuming conductive cooling and assuming a representative surface temperature of 60 K, and shown for a series of different temperatures at the ice/ocean interface. The horizontal purple shaded bands illustrate the 1σ (dark) and 2σ (pale) ranges of likely ice shell thicknesses (Fig. 4g). The vertical gray band represents the internal dissipation permitted assuming the present-day effective dissipation within Saturn corresponds to $1000 < Q < 4000$, with the dashed line representing $Q = 2000$ (Fuller et al., 2016; Lainey et al., 2012). (For interpretation of the references to color in this figure legend, the reader is referred to the web version of this article.)

ocean produces an altogether distinct pattern, with maximum dissipation at the equator, especially at the centers of the leading and trailing hemispheres, and minimum dissipation at the poles, leading to a shell that is thinnest at the equator and thickest at the poles (Matsuyama et al., 2018). Moreover, such dissipation may only be a few $\times 10^{-6}\ \text{W/m}^2$ (~ 2 MW in total), some four orders of magnitude smaller than the value corresponding to the inferred shell thickness (Fig. 11b). Obliquity tides produce heating that is maximal at the poles but the magnitude is at least four orders of magnitude too small, when adopting the parameters considered by Matsuyama et al. (2018). More significant dissipation within the ocean may be possible, especially if turbulence is important at the ocean boundaries where the topography may be rough (Wilson and Kerswell, 2018), or due to resonant waves that may occur in the ocean (Lemasquerier et al., 2017), though further studies on these phenomena are needed.

Tidal dissipation within the rocky core may occur in a pattern similar to what is expected for heating within the ice shell (Choblet et al., 2017), but that heat must then be transported through the ocean, which could significantly alter or remove lateral variations in the heat supplied to the base of the ice shell. If the ocean is not stratified, narrow plumes may occur over the most strongly heated parts of the core, leading to localized ice shell thinning (e.g., Goodman et al., 2004; Goodman and Lenferink, 2012; Vance and Goodman, 2009). If the most strongly heated parts of the core are at the poles (Choblet et al., 2017), this could help explain the thinner ice in the polar regions. Such polar upwellings would not, however, account for the longitudinal variations in the shell's structure. Upwellings could also be disrupted by any convection that may be taking place within the ocean. And if convection in the ocean is sufficiently vigorous, the heat supplied to the ice shell could in fact be concentrated at low latitudes (Soderlund et al., 2014), which would be inconsistent with the ice shell being thickest near the equator. Although it is not known whether or not the ocean is stratified, the presence of salts and nanosilica grains in the ocean (Hsu et al., 2015; Postberg et al., 2011) along with the likely ongoing freezing and melting at the ocean-ice interface (e.g., Čadek et al., 2017, 2019) could lead to brine rejection at low latitudes and ponding of fresh water at the poles. Such processes may lead to ocean stratification which would inhibit direct radial heat transport between the core and the ice shell. If the ocean is indeed stratified, the heat emerging from the core may be efficiently redistributed within the ocean, resulting in a nearly uniform distribution of heat supplied to the base of the ice shell, at least on the large scales we consider here, and therefore not contributing to global scale shell thickness variations. Hence, although some degree of tidal dissipation probably occurs within the ocean and the core, it is not clear that either of these modes of internal heat production could account for the inferred pattern of shell thickness variations (Fig. 11d). We therefore argue that tidal dissipation within the ice shell itself is likely an important component of internal heat production.

4.3. Discussion

Although our ice shell tidal heating model and our new interior model exhibit broadly consistent ice shell structures, a few caveats should be considered. Because our tidal heating model computes dissipation in a thin, symmetric shell, with dissipation being related to the squares of the strain rates arising from the time varying degree-2 tidal stresses (Ojakangas and Stevenson, 1989), the model predicts a symmetric pattern with power only up to spherical harmonic degree 4. Consequently, the model does not predict many of the shorter wavelength features, nor the south polar anomaly. Even neglecting these anomalies, our tidal heating model slightly underestimates the amplitude of the lateral shell thickness variations.

Our calculation of the equilibrium ice shell structure also neglects the effect of any ongoing viscous relaxation. The lateral shell thickness variations create lateral pressure gradients, which will cause secular flow in the low viscosity region near the base of the ice shell (e.g., Čadek et al., 2017, 2019; Kamata and Nimmo, 2017), which will tend to remove the lateral thickness variations. The resulting imbalance between conductive heat loss and local tidal dissipation will cause ocean

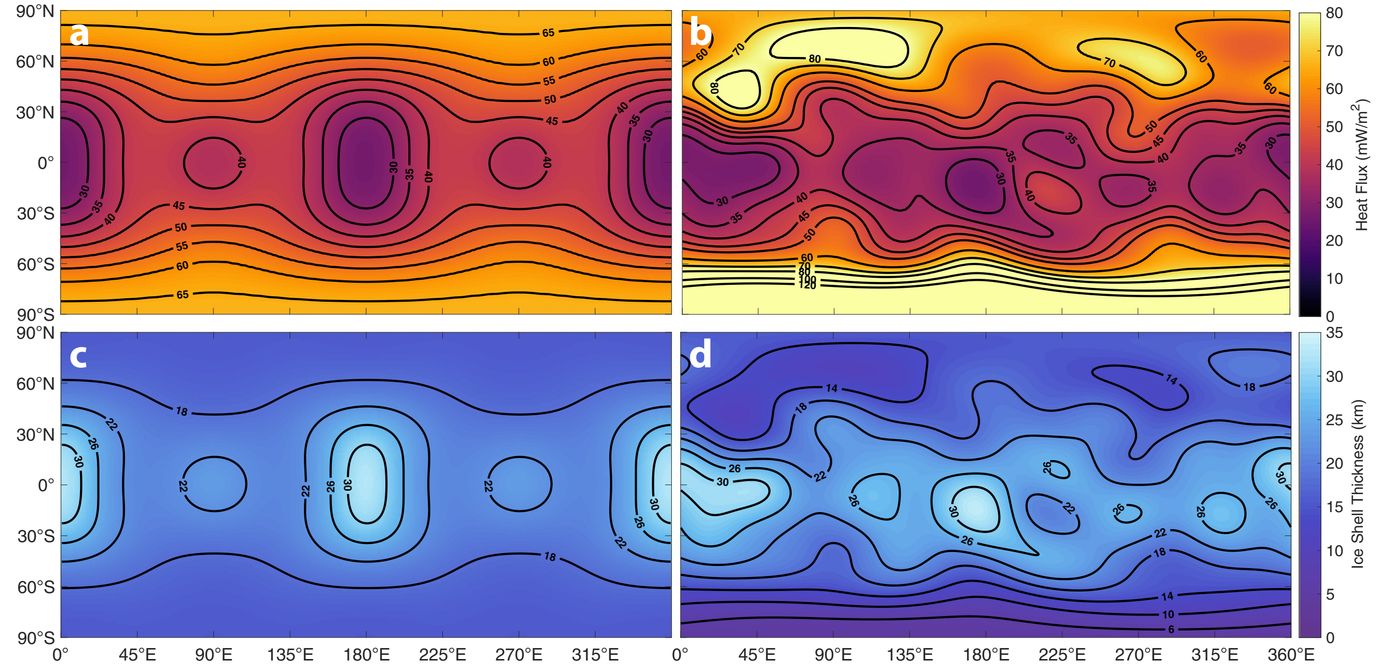

Fig. 11. Comparison between predicted and inferred shell structure and heat flux. (a) Predicted pattern of tidal dissipation and (c) the corresponding equilibrium ice shell structure when the total dissipation is ~35 GW such that the mean shell thickness is 21 km. (b) Conductive heat loss corresponding to (d) the nominal inferred shell structure, with mean shell and ocean thicknesses of 21 km and 37 km, respectively (Fig. 4g), as derived from the newer shape model (Tajeddine et al. 2017), truncated to spherical harmonic degree 8.

freezing beneath the thickest parts of the shell and basal melting at the thinnest parts of the shell. Taking this effect into account should further mute the expected lateral shell thickness variations, making the large amplitude of the inferred thickness variations yet more difficult to explain. On the other hand, our model also assumes that tidal dissipation occurs in a uniform thin shell whereas, in reality, dissipation should be enhanced in the thinner parts of the shell near the poles (Běhounková et al., 2017; Beuthe, 2018; Soucek et al., 2016)—a feedback that will lead to larger amplitude shell thickness variations. Similarly, because our tidal dissipation model assumes no ongoing freezing and melting, it is an approximation that is only valid if the rate of freezing and melting is sufficiently slow—as it must be in order to maintain significant lateral shell thickness variations (see also Čadek et al., 2017, 2019; Kvorka et al., 2018).

A related problem is that the ice must have a rheology that permits the required ~35 GW of heat dissipation without having a basal viscosity that is too low to maintain shell thickness variations. For example, to dissipate 35 GW using the Efroimsky (2018) model (which, for simplicity, assumes a uniform interior), and using an Andrade rheology (e.g., Shoji et al., 2013), would require a viscosity of $\sim 10^{13}$ Pa · s, depending on the assumed shear modulus. While such a viscosity is not unreasonable for water ice near its melting temperature, Čadek et al. (2019) argue that if the basal viscosity is less than $\sim 3 \times 10^{14}$ Pa · s, viscous relaxation would be too rapid to be balanced by ongoing freezing and melting. We note, however, that viscous relaxation and tidal dissipation occur on very different timescales (millions of years versus 1.37 days) and given that the two processes may involve different mechanisms (e.g., dislocation creep versus grain sliding) and very different strain rates, the relevant effective viscosities could be somewhat different (see also McCarthy and Cooper, 2016). An advantage of core dissipation models (e.g., Choblet et al., 2017), of course, is that high viscosities in the ice shell are not problematic because dissipation in the ice shell is not required, as long as the core itself can be sufficiently dissipative at tidal frequencies—a matter that still requires experimental validation (see Methods of Choblet et al., 2017). In any case, further work is needed to identify realistic rheologies that can deliver the required dissipation, whether in the ice shell or the core, within the context of a realistic three-dimensional model for Enceladus.

Finally, even when we assume that the tidal dissipation in the ice shell is sufficient to produce a mean ice shell thickness of 21 km, the expected dissipation pattern (Fig. 11a) slightly underestimates the heat flux corresponding to the inferred shell structure (Fig. 11b) in certain areas, such as at mid northern latitudes and particularly in the south polar region, where the inferred heat flux is approximately twice what is predicted by the model (Fig. S6). This could be explained in part by the fact that our tidal dissipation model assumes a uniform shell thickness whereas dissipation should be enhanced in the thinner parts of the shell (Beuthe, 2018; Soucek et al., 2016). Because we have set the magnitude of the dissipation to produce the desired mean shell thickness, there are naturally also regions where the model overestimates the heat flux slightly. It should be noted that the most significant excess heating is confined to a region poleward of roughly $70^{\circ} S$, accounting for just 3% of the surface area, such that the total heat anomaly illustrated in Fig. S6 is only ~3 GW. In reality, the conductive heat loss in the south polar region may be even less than 3 GW due to the elevated surface temperatures (Howett et al., 2011; Spencer et al., 2013) and correspondingly shallower geothermal gradients. Of course, the total heat loss is likely somewhat greater, however, due to the advective heat loss associated with the eruptions.

5. Conclusions

Determining the structure of Enceladus's ice shell is challenging in part because the analysis is sensitive to factors such as the approach to computing the reference hydrostatic equilibrium figure and the ways in which flexural and isostatic support are modeled (see section 3.2.2). After an exhaustive parameter space exploration, and employing a numerically accurate approach to calculating the equilibrium figures (section 2.2; Tricarico, 2014), we have obtained a new interior model (Figs. 4 and 9) that satisfies the observational constraints using the Hemingway and Matsuyama (2017) approach to Airy isostasy (section 2.3), which is meant to eliminate lateral pressure gradients at depth, and without the need for elastic support (sections 2.4 and 3.2.5; *cf.* Čadek et al., 2016).

The ice shell is sufficiently thin that conductive heat loss significantly exceeds the already large ~5 GW associated with the eruptions along the Tiger Stripe fractures (Howett et al., 2011; Spencer et al., 2013). We find that global conductive heat loss alone is in the range of 20 − 35 GW, far in excess of radiogenic heating and tidal dissipation when traditional assumptions about tidal interactions with Saturn and Dione are adopted (Meyer and Wisdom, 2007, 2008). Whereas this would imply a rapidly freezing ocean, recent astrometric observations (Lainey et al., 2012, 2017) suggest that much greater tidal dissipation is possible (~25 GW assuming $Q_{\text{Saturn}} = 2000$) and, allowing for the resonance locking mechanism of Fuller et al. (2016), is compatible with long-lived Saturnian satellites. Hence, although a balanced heat budget is not assured, it is at least possible, meaning that the interior of Enceladus could be close to a steady state, permitting a long-lived internal liquid water ocean.

The implied shell structure (Fig. 11d) resembles the spatial pattern expected if tidal dissipation occurs primarily near the base of the ice shell (Fig. 11c). By contrast, tidal heating within the subsurface ocean (Matsuyama et al., 2018) may not be able to account for the observed shell thickness variations both because the spatial pattern does not match and because the amplitude is orders of magnitude too small (section 4.2). Whereas tidal dissipation within the core could—if the ocean is not stratified—contribute to ice shell thinning at the poles (Choblet et al., 2017), it cannot easily account for the inferred longitudinal variations in shell thickness, unless the core heat can be effectively transported radially outward through the ocean without inducing ocean currents that would alter the spatial pattern. We therefore conclude that tidal dissipation within the ice shell itself must be an important mode of internal heat production (section 4.2).

Although our tidal heating model and our new interior model exhibit broadly consistent ice shell structures, future work is required to determine the likely equilibrium between the opposing effects of viscous relaxation (e.g., Čadek et al., 2017, 2019) and enhanced dissipation in the thinner parts of the shell (Běhounková et al., 2017; Beuthe, 2018) (section 4.3). Future measurements of heat flux outside the SPT, observations of higher order terms in the gravitational field, and measurement of gravitational field variations over orbital timescales, could help to further constrain the ice shell's structure and its implications for the past and future evolution of Enceladus.

Acknowledgments

This research was funded primarily by the Miller Institute for Basic Research in Science at the University of California, Berkeley, and was made possible by the NASA/ESA Cassini mission to Saturn and, in particular, the work of the Radio Science and Imaging Science Subsystem teams. We thank Francis Nimmo, Ondřej Čadek, and Anton Ermakov for their thorough and constructive reviews. This work also benefited from discussions with Michael Beuthe, Bruce Buffett, Michael Manga, Bill McKinnon, Naor Movshovitz, Radwan Tajeddine, and Gabriel Tobie. We thank Daniele Durante and Luciano Iess for supplying the covariance matrix corresponding to the estimated gravitational potential coefficients. All other data are publicly available in the published literature.

Appendix A. Flexural support

We obtain Eqs. (14) and (15) following previous work (Kraus, 1967; Turcotte et al., 1981), but with several assumptions relaxed or altered to better suit the present problem. Treating the lithosphere as a uniform thin elastic shell (Kraus, 1967; Turcotte et al., 1981; Willemann and Turcotte, 1982), we can write the pressure (p_w) associated with the elastic restoring stresses resulting from the deflection of the shell (w) as

$$D\nabla^6 w + 4D\nabla^4 w + 4D\nabla^2 w + ET_e R^2\nabla^2 w + 2ET_e R^2 w - R^4(\nabla^2 + 1 - \nu)p_w = 0 \tag{37}$$

where D represents flexural rigidity and is given by

$$D = \frac{ET_e^3}{12(1-\nu^2)} \tag{38}$$

where T_e is the effective elastic thickness, E is Young's modulus, and ν is Poisson's ratio, and where ∇^2 is the Laplacian operator. R is the radius of the thin elastic shell, which we take to be the body's outer radius. Here we have taken w as positive upward deflection of the elastic shell, and p_w as positive downward pressure. Hence, p_w and w must have the same sign in order to satisfy Eq. (37); positive upward deflection results in a positive downward restoring pressure. Note that Turcotte et al. (1981) use a different convention in their Eq. (1) with the deflection, w, being positive downward and with their pressure term referring to the applied pressure rather than the elastic response of the shell. Note also that, as pointed out by Willemann and Turcotte (1982), Turcotte et al. (1981) neglected to include the third term in Eq. (37), which has a small effect on our Eq. (43).

To balance the pressures at depth beneath unloaded and loaded portions of the shell, we use Eq. (3) from Hemingway and Matsuyama (2017), except that we additionally include the effects of the elastic restoring stress. The result is

$$p_w = -(\Delta\rho g_b h_b + \rho_c g_t h_t) \tag{39}$$

where, h_t and h_b are, respectively, the (positive upward) topographic relief at the top and bottom of the ice shell, measured with respect to the hypothetical equilibrium figure (i.e., h_t and h_b are the non-hydrostatic topography), where ρ_c is the density of the shell, $\Delta\rho$ is the density contrast between the shell and the ocean, and g_t and g_b are the mean gravitational accelerations at the top and bottom of the shell, respectively.

Eq. (39) differs from Eq. (3) of Turcotte et al. (1981) in three ways. First, there are differences of sign convention, as discussed. Second, we account for the possibility that the gravitational acceleration may vary between the top and bottom of the shell (this can be important for Enceladus; see Hemingway and Matsuyama, 2017). Finally, we do not include the effects of self-gravitation. While self-gravitation of the relief does affect the local equipotential surfaces, it does not make sense to alter Eq. (39) by the elevation of the geoid at the surface. As pointed out by Hemingway and Matsuyama (2017), the goal is not to balance the weight of surface topography against the buoyancy of basal topography. Instead, what is important is the accumulation of pressure at depth computed via integration of the hydrostatic equation. A datum equipotential surface at depth will experience elevation changes due to the surface relief and the compensating basal relief (only the former of which is addressed by adding the geoid elevation to Eq. (39)). But at long wavelengths, even with significant elastic support, the compensation is large enough that the effects of the surface and basal relief largely cancel, meaning that the datum equipotential surface elevation can be taken as fixed, and can therefore be neglected in Eq. (39).

In this model, the topographic relief at the top and bottom of the ice shell (h_t and h_b, respectively) are a function of the thickening or thinning of the shell and the resulting lithospheric deflection (w). Thickening or thinning can occur due to: excavation of surface material due to impacts; sediment transport; emplacement of surface loads due to volcanism; viscous relaxation; tectonic spreading or compression; or freezing or melting at the base of the ice shell. If the load thicknesses at the top and bottom of the shell are d_t and d_b, respectively, with positive values indicating thickening and negative values indicating thinning, then (neglecting radial compression of the loaded shell) the topographic relief at the top and bottom of the shell can be written

$$h_t = w + d_t \tag{40}$$

$$h_b = w - d_b. \tag{41}$$

For clarity and simplicity, we have not included the subscripts *lm* in the above expressions but these should be taken as the amplitudes of periodic functions and the solutions here apply to individual spherical harmonic degrees and orders. We also assume that the periodic loads, d_t and d_b, and the resulting lithospheric deflection, w, and topographic relief, h_t and h_b, are all in-phase—a good assumption when the loading is either purely from the top or purely from the bottom.

Making use of the geometric constraints of Eqs. (40) and (41), and the requirement of equal pressures at depth (39), we can solve Eq. (37) for the deflection, w, obtaining

$$w = \frac{\Delta\rho g_b d_b - \rho_c g_t d_t}{\Delta\rho g_b + \rho_c g_t + \zeta} \tag{42}$$

where we have introduced an additional parameter, ζ, which has units of force per unit volume and will serve as a shorthand for the flexural rigidity at a particular wavelength, and is given by

$$\zeta(l, R, E, T_e, \nu) = \frac{ET_e}{R^2}\left(\frac{\frac{T_e^2}{R^2 12(1-\nu^2)}(l^3(l+1)^3 - 4l^2(l+1)^2 + 4l(l+1)) + l(l+1) - 2}{l(l+1) - (1-\nu)}\right) \tag{43}$$

where we have replaced each ∇^2 with $-l(l+1)$ (Turcotte et al., 1981; Willemann and Turcotte, 1982). Here again, R is the body's outer radius.

For finite rigidity ($\zeta < \infty$), and if both h_t and d_b are specified, then combining Eqs. (40), (41), and (42), it can be shown that

$$h_b = -h_t \frac{\rho_c}{\Delta\rho}\frac{g_t}{g_b}\left(\frac{1 + \frac{d_b}{h_t}\frac{\zeta}{\rho_c g_t}}{1 + \frac{\zeta}{\Delta\rho g_b}}\right). \tag{44}$$

Similarly, if $\zeta < \infty$, and both h_t and d_t are specified, then it can be shown that

$$h_b = -h_t \frac{\rho_c}{\Delta\rho}\frac{g_t}{g_b}\left(1 + \frac{\zeta}{\rho_c g_t}\left(1 - \frac{d_t}{h_t}\right)\right). \tag{45}$$

This expression corresponds to Eq. (S23) of Hemingway et al. (2013) except that here we allow for the radial variation in gravity and we do not assume equal masses in columns of equal width (see Hemingway and Matsuyama, 2017).

For non-zero rigidity, and if the loading is entirely at the top of the shell, then $d_b = 0$ and Eq. (44) reduces to

$$h_b = -h_t \frac{\rho_c}{\Delta\rho}\frac{g_t}{g_b}(C_t) \tag{46}$$

or, when the loading is entirely at the base of the shell, and $d_t = 0$, Eq. (45) reduces to

$$h_b = -h_t \frac{\rho_c}{\Delta\rho}\frac{g_t}{g_b}\left(\frac{1}{C_b}\right). \tag{47}$$

In these expressions, C_t and C_b are compensation factors corresponding to the cases of top and bottom loading, respectively, and are given by

$$C_t = \frac{1}{1 + \frac{\zeta}{\Delta\rho g_b}} \tag{48}$$

and

$$C_b = \frac{1}{1 + \frac{\zeta}{\rho_c g_t}}. \tag{49}$$

In both cases, decreasing rigidity ($T_e \to 0$, $\zeta \to 0$) leads the compensation factor to approach unity. In the case of zero rigidity, both Eqs. (44) and (45) reduce to Eq. (12). For non-zero rigidity, the compensation factors mean different things for the cases of bottom and top loading. An infinitely rigid shell ($T_e \to \infty$, $\zeta \to \infty$) leads to zero compensation ($C = 0$) in either case, but that means zero root thickness in the case of top loading or zero surface relief in the case of bottom loading. For a finite elastic thickness, $0 < T_e < \infty$, in general $C_t \neq C_b$. When g_t/g_b is assumed to be unity, our Eq. (46) is identical to Eq. (21) of Turcotte et al. (1981), except that our ζ incorporates the term that was missing from Eq. (1) of Turcotte et al. (1981) (Willemann and Turcotte, 1982).

Appendix B. Supplementary data

Supplementary data to this article can be found online at https://doi.org/10.1016/j.icarus.2019.03.011.

References

Běhounková, M., Souček, O., Hron, J., Čadek, O., 2017. Plume activity and tidal deformation on Enceladus influenced by faults and variable ice shell thickness. Astrobiology. https://doi.org/10.1089/ast.2016.1629.(ast.2016.1629. URL: http://online.liebertpub.com/doi/10.1089/ast.2016.1629).

Besserer, J., Nimmo, F., Roberts, J.H., Pappalardo, R.T., 2013. Convection-driven compaction as a possible origin of Enceladus's long wavelength topography. Journal of Geophysical Research E: Planets 118, 908–915. https://doi.org/10.1002/jgre.20079.

Beuthe, M., 2018. Enceladus's crust as a non-uniform thin shell: I tidal deformations. Icarus 302, 145–174. https://doi.org/10.1016/j.icarus.2017.11.009. doi:10.1016/j.icarus.2017.11.009. arXiv:1711.08236.

Beuthe, M., Rivoldini, A., & Trinh, A. (2016). Enceladus' and Dione's floating ice shells supported by minimum stress isostasy. Geophys. Res. Lett., URL: http://doi.wiley.com/10.1002/2016GL070650. doi:https://doi.org/10.1002/2016GL070650.

Bland, M.T., Beyer, R.A., Showman, A.P., 2007. Unstable extension of Enceladus' lithosphere. Icarus 192, 92–105. https://doi.org/10.1016/j.icarus.2007.06.011.

Čadek, O., Tobie, G., Hoolst, T.V., Mass, M., Choblet, Gael, Lefevre, A., Mitri, G., Baland, R.-m., Běhounková, M., Bourgeois, O., Trinh, A., 2016. Enceladus's internal ocean and ice shell constrained from Cassini gravity, shape and libration data. Geophys. Res. Lett. https://doi.org/10.1002/2016GL068634.

Čadek, O., Běhounková, M., Tobie, G., Choblet, G., 2017. Viscoelastic relaxation of Enceladus's ice shell. Icarus 291, 31–35. https://doi.org/10.1016/j.icarus.2017.03.011.

Čadek, O., Souček, O., Běhounková, M., Choblet, G., Tobie, G., Hron, J., 2019. Long-term stability of Enceladus' uneven ice shell. Icarus 319, 476–484.. URL: https://www.sciencedirect.com/science/article/pii/S0019103518303762. https://doi.org/10.1016/J.ICARUS.2018.10.003.

Choblet, G., Tobie, G., Sotin, C., Běhounková, M., Čadek, O., Postberg, F., Souček, O., 2017. Powering prolonged hydrothermal activity inside Enceladus. Nature Astronomy. https://doi.org/10.1038/s41550-017-0289-8. URL: http://www.nature.com/articles/s41550-017-0289-8.

Crow-Willard, E.N., Pappalardo, R.T., 2015. Structural mapping of Enceladus and implications for formation of tectonized regions. Journal of Geophysical Research: Planets 120, 928–950. https://doi.org/10.1002/2014JE004627.Received.

Darwin, G.H., 1899. The theory of the figure of the earth carried to the second order of small quantities. Mon. Not. R. Astron. Soc. 60, 82–124.

Efroimsky, M., 2018. Dissipation in a tidally perturbed body librating in longitude. Icarus 306, 328–354. URL: https://doi.org/10.1016/j.icarus.2017.10.020 doi:10.1016/j.icarus.2017.10.020. arXiv:1706.08999.

Fuller, J., Luan, J., Quataert, E., 2016. Resonance locking as the source of rapid tidal migration in the Jupiter and Saturn moon systems. Mon. Not. R. Astron. Soc. 458, 3867–3879. http://arxiv.org/abs/1601.05804 https://doi.org/10.1093/mnras/stw609 arXiv:1601.05804.

Giese, B., Wagner, R., Hussmann, H., Neukum, G., Perry, J., Helfenstein, P., Thomas, P.C., 2008. Enceladus: an estimate of heat flux and lithospheric thickness from flexurally supported topography. Geophys. Res. Lett. 1–5. https://doi.org/10.1029/2008GL036149.

Goodman, J.C., Lenferink, E., 2012. Numerical simulations of marine hydrothermal plumes for Europa and other icy worlds. Icarus 221, 970–983. https://www.sciencedirect.com/science/article/pii/S0019103512003466. https://doi.org/10.1016/J.ICARUS.2012.08.027.

Goodman, J.C., Collins, G.C., Marshall, J., Pierrehumbert, R.T., 2004. Hydrothermal plume dynamics on Europa: implications for chaos formation. J. Geophys. Res. https://doi.org/10.1029/2003JE002073. URL: http://doi.wiley.com/10.1029/2003JE002073.

Hemingway, D.J., Matsuyama, I., 2017. Isostatic equilibrium in spherical coordinates and implications for crustal thickness on the Moon, Mars, Enceladus, and elsewhere. Geophys. Res. Lett. 7695–7705. https://doi.org/10.1002/2017GL073334.

Hemingway, D.J., Nimmo, F., Iess, L., 2013. Enceladus' internal structure inferred from analysis of Cassini-derived gravity and topography. In: *AGU Fall Meeting 2013* P53E-03.

Howett, C.J.A., Spencer, J.R., Pearl, J., Segura, M., 2011. High heat flow from Enceladus' south polar region measured using 10-600 cm-1 Cassini/CIRS data. Journal of Geophysical Research E: Planets 116, 1–15. https://doi.org/10.1029/2010JE003718.

Hsu, H.-W., Postberg, F., Sekine, Y., Shibuya, T., Kempf, S., Horányi, M., Juhász, A., Altobelli, N., Suzuki, K., Masaki, Y., Kuwatani, T., Tachibana, S., Sirono, S.-i., Moragas-Klostermeyer, G., Srama, R., 2015. Ongoing hydrothermal activities within Enceladus. Nature 519, 207–210. http://www.nature.com/doifinder/10.1038/nature14262 https://doi.org/10.1038/nature14262.

Iess, L., Stevenson, D.J., Parisi, M., Hemingway, D.J., Jacobson, R.A., Lunine, J.I., Nimmo, F., Armstrong, J.W., Asmar, S.W., Ducci, M., Tortora, P., 2014. The gravity field and interior structure of Enceladus. Science (New York, N.Y.) 78–80. URL: http://www.sciencemag.org/cgi/doi/10.1126/science.1250551. https://doi.org/10.1126/science.1250551.

Ingersoll, A.P., Nakajima, M., 2016. Controlled boiling on Enceladus. 2. Model of the liquid-filled cracks. Icarus 272, 319–326. https://doi.org/10.1016/j.icarus.2015.12.040.

Kamata, S., Nimmo, F., 2017. Interior thermal state of Enceladus inferred from the viscoelastic state of the ice shell. Icarus 284, 387–393. URL. https://doi.org/10.1016/j.icarus.2016.11.034 (doi:10.1029/2011JE003835).

Kite, E.S., Rubin, A.M., 2016. Sustained eruptions on Enceladus explained by turbulent dissipation in tiger stripes. Proc. Natl. Acad. Sci. 113, 201520507. URL: http://www.pnas.org/lookup/doi/10.1073/pnas.1520507113. https://doi.org/10.1073/pnas.1520507113.

Kraus, H., 1967. Thin Elastic Shells. Wiley, New York.

Kvorka, J., Čadek, O., Tobie, G., Choblet, G., 2018. Does Titan's long-wavelength topography contain information about subsurface ocean dynamics? Icarus 310, 149–164. https://doi.org/10.1016/j.icarus.2017.12.010.

Lainey, V., Karatekin, Ö., Desmars, J., Charnoz, S., Arlot, J.-E., Emelyanov, N., Le Poncin-Lafitte, C., Mathis, S., Remus, F., Tobie, G., Zahn, J.-P., 2012. Strong tidal dissipation in Saturn and constraints on Enceladus' thermal state from astrometry. Astrophys. J. https://doi.org/10.1088/0004-637X/752/1/14. http://stacks.iop.org/0004-637X/752/i = 1/a = 14?key = crossref.d68a903d62213eb4f281cc2f4669349f.

Lainey, V., Jacobson, R.A., Tajeddine, R., Cooper, N.J., Murray, C., Robert, V., Tobie, G., Guillot, T., Mathis, S., Remus, F., Desmars, J., Arlot, J.-E., De Cuyper, J.-P., Dehant, V., Pascu, D., Thuillot, W., Poncin-Lafitte, C.L., Zahn, J.-P., 2017. New constraints on Saturn's interior from Cassini astrometric data. Icarus 281, 286–296. http://linkinghub.elsevier.com/retrieve/pii/S0019103516304183 https://doi.org/10.1016/j.icarus.2016.07.014.

Lambeck, K., 1988. Geophysical Geodesy: The Slow Deformations of the Earth. Oxford University Press, New York.

Lemasquerier, D., Grannan, A.M., Vidal, J., Cébron, D., Favier, B., Le Bars, M., Aurnou, J.M., 2017. Libration-driven flows in ellipsoidal shells. Journal of Geophysical Research: Planets 122, 1926–1950. URL: http://doi.wiley.com/10.1002/2017JE005340. https://doi.org/10.1002/2017JE005340.

Manga, M., Wang, C.Y., 2007. Pressurized oceans and the eruption of liquid water on Europa and Enceladus. Geophys. Res. Lett. 1–5. https://doi.org/10.1029/2007GL029297.

Matsuyama, I., Beuthe, M., Hay, H.C., Nimmo, F., Kamata, S., 2018. Ocean tidal heating in icy satellites with solid shells. Icarus 312, 208–230. https://doi.org/10.1016/j.icarus.2018.04.013. doi:10.1016/j.icarus.2018.04.013. arXiv:1804.07727.

McCarthy, C., Cooper, R.F., 2016. Tidal dissipation in creeping ice and the thermal evolution of Europa. Earth Planet. Sci. Lett. 443, 185–194.

McKinnon, W.B., 2013. The shape of Enceladus as explained by an irregular core: implications for gravity, libration, and survival of its subsurface ocean. Journal of Geophysical Research: Planets 118https://doi.org/10.1002/jgre.20122. http://doi.wiley.com/10.1002/jgre.20122.

McKinnon, W.B., 2015. Effect of Enceladus's rapid synchronous spin on interpretation of Cassini gravity. Geophys. Res. Lett. https://doi.org/10.1002/2015GL063384.

Meyer, J., Wisdom, J., 2007. Tidal heating in Enceladus. Icarus 188, 535–539. http://linkinghub.elsevier.com/retrieve/pii/S0019103507001054 https://doi.org/10.1016/j.icarus.2007.03.001.

Meyer, J., Wisdom, J., 2008. Tidal evolution of Mimas, Enceladus, and Dione. Icarus 193, 213–223. https://doi.org/10.1016/j.icarus.2007.09.008.

Murray, C.D., Dermott, S., 1999. Solar System Dynamics. Cambridge University Press.

Nadeau, A., Mcgehee, R., 2017. A simple formula for a planet's mean annual insolation by latitude. Icarus 291, 46–50. https://doi.org/10.1016/j.icarus.2017.01.040.

Nakajima, M., Ingersoll, A.P., 2016. Controlled boiling on Enceladus. 1. Model of the vapor-driven jets. Icarus 272, 309–318. https://doi.org/10.1016/j.icarus.2016.02.027.

Nimmo, F., Thomas, P.C., Pappalardo, R.T., Moore, W.B., 2007. The global shape of Europa: constraints on lateral shell thickness variations. Icarus 191, 183–192. https://doi.org/10.1016/j.icarus.2007.04.021.

Nimmo, F., Bills, B.G., Thomas, P.C., 2011. Geophysical implications of the long-wavelength topography of the Saturnian satellites. J. Geophys. Res. E11001. http://doi.wiley.com/10.1029/2011JE003835 https://doi.org/10.1029/2011JE003835.

Nimmo, F., Porco, C., Mitchell, C., 2014. Tidally modulated eruptions on Enceladus: Cassini ISS observations and models. Astron. J. 46. http://stacks.iop.org/1538-3881/148/i = 3/a = 46?key = crossref.aa4e6bbc50ecc4ba5aec7e3316ec9995 https://doi.org/10.1088/0004-6256/148/3/46.

Nimmo, F., Barr, A. C., Běhounková, M., & Mckinnon, W. B. (2018). The thermal and orbital evolution of Enceladus: observational constraints and models. In P. M. Schenk, R. N. Clark, C. J. A. Howett, & A. J. Verbiscer (Eds.), Enceladus and the Icy Moons of Saturn (pp. 79–94). Tucson, Arizona: University of Arizona Press. https://websites.pmc.ucsc.edu/ fnimmo/website/Enceladus_in_press.pdf.

Ojakangas, G.W., Stevenson, D.J., 1989. Thermal state of an ice shell on Europa. Icarus 81, 220–241. https://doi.org/10.1016/0019-1035(89)90053-5.

Peale, S., Cassen, P., 1978. Contribution of tidal dissipation to lunar thermal history. Icarus 36, 245–269. http://www.sciencedirect.com/science/article/pii/0019103578901094 https://doi.org/10.1016/0019-1035(78)90109-4.

Petrenko, V.F., Whitworth, R.W., 1999. Physics of Ice. Oxford University Press.

Porco, C.C., Helfenstein, P., Thomas, P.C., Ingersoll, A.P., Wisdom, J., West, R., Neukum, G., Denk, T., Wagner, R., Roatsch, T., Kieffer, S., Turtle, E., McEwen, A., Johnson, T.V., Rathbun, J., Veverka, J., Wilson, D., Perry, J., Spitale, J., Brahic, A., Burns, J.A., Delgenio, A.D., Dones, L., Murray, C.D., Squyres, S., 2006. Cassini observes the active south pole of Enceladus. Science 1393–1401. *(New York, N.Y.)*. http://www.ncbi.nlm.nih.gov/pubmed/16527964. https://doi.org/10.1126/science.1123013.

Postberg, F., Schmidt, J., Hillier, J., Kempf, S., Srama, R., 2011. A salt-water reservoir as the source of a compositionally stratified plume on Enceladus. Nature 474, 620–622. http://www.nature.com/doifinder/10.1038/nature10175 https://doi.org/10.1038/nature10175.

Richard, A., Rambaux, N., Charnay, B., 2014. Librational response of a deformed 3-layer Titan perturbed by non-Keplerian orbit and atmospheric couplings. Planetary and Space Science 94, 22–34. URL: https://doi.org/10.1016/j.pss.2014.02.006 (doi:10.1016/j.pss.2014.02.006. arXiv:arXiv:1402.2493v1).

Roberts, J.H., 2015. The fluffy core of Enceladus. Icarus 258, 54–66. http://linkinghub.elsevier.com/retrieve/pii/S001910351500250X https://doi.org/10.1016/j.icarus.2015.05.033.

Roberts, J.H., Nimmo, F., 2008. Tidal heating and the long-term stability of a subsurface ocean on Enceladus. Icarus 194, 675–689. http://linkinghub.elsevier.com/retrieve/

pii/S0019103507005593 https://doi.org/10.1016/j.icarus.2007.11.010.

Rudolph, M.L., Manga, M., 2009. Fracture penetration in planetary ice shells. Icarus 199, 536–541. URL: https://doi.org/10.1016/j.icarus.2008.10.010 (doi:10.1016/j.icarus.2008.10.010).

Schenk, P.M., McKinnon, W.B., 2009. One-hundred-km-scale basins on Enceladus: evidence for an active ice shell. Geophys. Res. Lett. https://doi.org/10.1029/2009GL039916. URL: http://www.agu.org/pubs/crossref/2009/2009GL039916.shtml.

Shoji, D., Hussmann, H., Kurita, K., Sohl, F., 2013. Ice rheology and tidal heating of Enceladus. Icarus 226, 10–19. doi:10.1016/j.icarus.2013.05.004. https://doi.org/10.1016/j.icarus.2013.05.004.

Soderlund, K.M., Schmidt, B.E., Wicht, J., Blankenship, D.D., 2014. Ocean-driven heating of Europa's icy shell at low latitudes. Nat. Geosci. 16–19. https://doi.org/10.1038/ngeo2021.

Soucek, O., Hron, J., Behounkova, M., Cadek, O., 2016. Effect of the tiger stripes on the deformation of Saturn's moon Enceladus. Geophys. Res. Lett. 43, 7417–7423. https://doi.org/10.1002/2016GL069415.

Spencer, J.R., Howett, C.J.A., Verbiscer, A., Hurford, T.A., Segura, M., Spencer, D.C., 2013. Enceladus heat flow from high spatial resolution thermal emission observations. In: European Planetary Science Congress. 8. pp. 840.

Spohn, T., Schubert, G., 2003. Oceans in the icy Galilean satellites of Jupiter? Icarus 161, 456–467. https://doi.org/10.1016/S0019-1035(02)00048-9.

Tajeddine, R., Rambaux, N., Lainey, V., Charnoz, S., Richard, A., Rivoldini, A., Noyelles, B., 2014. Constraints on Mimas' interior from Cassini ISS libration measurements. Science 346, 322–324.

Tajeddine, R., Soderlund, K.M., Thomas, P.C., Helfenstein, P., Hedman, M.M., Burns, J.A., Schenk, P.M., 2017. True polar wander of Enceladus from topographic data. Icarus 295, 46–60. http://linkinghub.elsevier.com/retrieve/pii/S001910351630584X https://doi.org/10.1016/j.icarus.2017.04.019.

Thomas, P., 2010. Sizes, shapes, and derived properties of the Saturnian satellites after the Cassini nominal mission. Icarus 208, 395–401. http://linkinghub.elsevier.com/retrieve/pii/S0019103510000448 https://doi.org/10.1016/j.icarus.2010.01.025.

Thomas, P., Tajeddine, R., Tiscareno, M., Burns, J., Joseph, J., Loredo, T., Helfenstein, P., Porco, C., 2016. Enceladus's measured physical libration requires a global subsurface ocean. Icarus 264, 37–47. http://linkinghub.elsevier.com/retrieve/pii/S0019103515003899 https://doi.org/10.1016/j.icarus.2015.08.037.

Tricarico, P., 2014. Multi-layer hydrostatic equilibrium of planets and synchronous moons: theory and application to Ceres and to solar system moons. Astrophys. J. 99. http://stacks.iop.org/0004-637X/782/i=2/a=99?key=crossref.51a63b8cfe5c9568438c8375874b01f7 https://doi.org/10.1088/0004-637X/782/2/99.

Turcotte, D.L., Willemann, R.J., Haxby, W.F., Norberry, J., 1981. Role of membrane stresses in the support of planetary topography. J. Geophys. Res. 3951–3959.

Van Hoolst, T., Rambaux, N., Karatekin, Ö., Baland, R.M., 2009. The effect of gravitational and pressure torques on Titan's length-of-day variations. Icarus 200, 256–264. https://doi.org/10.1016/j.icarus.2008.11.009.

Van Hoolst, T., Baland, R.M., Trinh, A., 2013. On the librations and tides of large icy satellites. Icarus 226, 299–315. https://doi.org/10.1016/j.icarus.2013.05.036.

Van Hoolst, T., Baland, R.-M., Trinh, A., 2016. The diurnal libration and interior structure of Enceladus. Icarus 277, 311–318. http://linkinghub.elsevier.com/retrieve/pii/S0019103516302020 https://doi.org/10.1016/j.icarus.2016.05.025.

Vance, S., Goodman, J., 2009. Oceanography of an Ice-Covered Moon. https://www.researchgate.net/publication/241525803.

Wieczorek, M., 2015. Gravity and topography of the terrestrial planets. In: Treatise on Geophysics, 2nd ed. Elsevier B.V, pp. 153–193. https://doi.org/10.1016/B978-0-444-53802-4.00169-X.

Wieczorek, M.A., Phillips, R.J., 1998. Potential anomalies on a sphere: applications to the thickness of the lunar crust. J. Geophys. Res. 1715–1724.

Willemann, R.J., Turcotte, D.L., 1982. The role of lithospheric stress in the support of the Tharsis rise. J. Geophys. Res. 9793–9801.

Wilson, A., Kerswell, R.R., 2018. Can libration maintain Enceladus's ocean? Earth Planet. Sci. Lett. 41–46. https://doi.org/10.1016/j.epsl.2018.08.012.